A MademoiseLLE domain binding platform links the key RNA transporter to endosomes

Senthil-Kumar Devan[1, $], Stephan Schott-Verdugo[2, 3, $], Kira Müntjes[1], Lilli Bismar[1], Jens Reiners[4], Eymen Hachani[5], Lutz Schmitt[5], Astrid Höppner[4], Sander HJ Smits[4, 5, *], Holger Gohlke[2, 3, *], Michael Feldbrügge[1, *]

$ shared first authorship

* shared corresponding authorship

[1] Institute of Microbiology, Heinrich Heine University Düsseldorf, Cluster of Excellence on Plant Sciences, 40204 Düsseldorf, Germany

[2] John von Neumann Institute for Computing (NIC), Jülich Supercomputing Centre (JSC), Institute of Biological Information Processing (IBI-7: Structural Bioinformatics), and Institute of Bio- and Geosciences (IBG-4: Bioinformatics), Forschungszentrum Jülich GmbH, Wilhelm-Johnen-Str., 52425 Jülich, Germany

[3] Institute for Pharmaceutical and Medicinal Chemistry, Heinrich Heine University Düsseldorf, Universitätsstraße 1, 40225 Düsseldorf, Germany

[4] Center for Structural Studies, Heinrich Heine University Düsseldorf, 40204 Düsseldorf, Germany

[5] Institute of Biochemistry I, Heinrich Heine University Düsseldorf, 40204 Düsseldorf, Germany

Running title: A novel MLLE platform

Key words: Endosome / PAM2 / Poly(A)-binding protein / RNA transport / *Ustilago maydis*

[*] **Corresponding authors:**

Dr. Sander HJ Smits

Institute of Biochemistry,

Heinrich Heine University Düsseldorf, 40204 Düsseldorf, Germany

Phone: +49 (211) 81-12647

sander.smits@hhu.de

Dr. Holger Gohlke
Institute for Pharmaceutical and Medicinal Chemistry,
Heinrich Heine University Düsseldorf, 40204 Düsseldorf, Germany
Phone: +49 (211) 81-13662
&
John von Neumann Institute for Computing (NIC), Jülich Supercomputing Centre (JSC), Institute of Biological Information Processing (IBI-7: Structural Bioinformatics), and Institute of Bio- and Geosciences (IBG-4: Bioinformatics), Forschungszentrum Jülich GmbH, 52425 Jülich, Germany
Phone: +49 (2461) 61-85550
gohlke@uni-duesseldorf.de & h.gohlke@fz-juelich.de
Dr. Michael Feldbrügge
Institute of Microbiology,
Bioeconomy Science Center, Cluster of Excellence on Plant Sciences
Heinrich Heine University Düsseldorf, 40204 Düsseldorf, Germany
Phone: +49 (211) 81-15475
feldbrue@hhu.de

Abstract

Spatiotemporal expression is mostly achieved by transport and translation of mRNAs at defined subcellular sites. An emerging mechanism mediating mRNA trafficking is microtubule-dependent co-transport of mRNAs on shuttling endosomes. Although progress has been made in identifying various components of the endosomal mRNA transport machinery, a mechanistic understanding of how these RNA-binding proteins are connected to endosomes is still lacking. Here, we demonstrate that a flexible MademoiseLLE (MLLE) domain platform within Rrm4 of *Ustilago maydis* is crucial for endosomal attachment. Our structure/function analysis uncovered three MLLE domains at the C-terminus of Rrm4 with a functionally defined hierarchy. MLLE3 recognizes two PAM2-like sequences of the adaptor protein Upa1 and is essential for endosomal shuttling of Rrm4. MLLE1 and MLLE2 are most likely accessory domains that exhibit a variant binding mode for interaction with currently unknown partners. Thus, endosomal attachment of the mRNA transporter is orchestrated by a sophisticated MLLE domain binding platform.

Introduction

mRNA localisation and local translation are essential for spatiotemporal control of protein expression. An important mechanism to achieve localised translation is the active transport of mRNAs along the cytoskeleton (Das *et al.*, 2021; Fernandopulle *et al.*, 2021; Mofatteh & Bullock, 2017). Mainly, long-distance transport of mRNA is mediated by motor-dependent movement along microtubules. Important carriers are transport endosomes that move messenger ribonucleoprotein complexes (mRNPs), consisting of RNA-binding proteins and cargo mRNAs on their cytoplasmic surface (Mofatteh & Bullock, 2017; Müntjes *et al.*, 2021; Niessing *et al.*, 2018). This process is evolutionarily conserved in fungi, plants, and animals (Baumann *et al.*, 2012; Cioni *et al.*, 2019; Tian *et al.*, 2020a; Liao *et al.*, 2019; Müntjes *et al..*, 2021; Quentin *et al.*, 2021; Schuhmacher *et al.*, 2021). In endosperm cells of developing rice seeds, cargo mRNAs are transported to cortical ER by the action of the two RNA recognition motif (RRM)-containing proteins RBP-P and RBP-L. These form a quaternary complex with membrane trafficking factor NSF (*N*-ethylmaleimide-sensitive factor) and small GTPase Rab5a on the endosomal surface (Tian *et al.*, 2020b). In neurons, mRNA transport has been linked to early and late endosomes as well as lysosomal vesicles. Especially, local translation of mRNAs encoding mitochondrial proteins on the surface of late endosomes is needed for mitochondrial function. Importantly, this trafficking process has been associated with the neuronal Charcot Marie-Tooth disease (Cioni *et al.*, 2019). Annexin 11, a factor implicated in amyotrophic lateral sclerosis (ALS), was found as an mRNP linker on motile lysosomal vesicles (Liao *et al.*, 2019). Recently, the five-membered FERRY complex was identified connecting mRNAs encoding mitochondrial proteins to neuronal endosomes by interaction with the active form of Rab5 (Quentin *et al.*, 2021; Schuhmacher *et al.*, 2021).

Among the best-studied examples for membrane-coupled mRNA transport is the endosomal mRNA transport in the corn pathogen *Ustilago maydis* (Béthune *et al.*, 2019; Haag *et al.*, 2015; Müntjes *et al.*, 2021). Extensive peripheral movement of mRNAs is needed for efficient unipolar growth of infectious hyphae. These hyphae grow highly polarised by expanding at the growing tip and inserting regularly spaced septa at the basal pole. Loss of mRNA distribution causes aberrant bipolar growth (Baumann *et al.*, 2012; Becht *et al.*, 2006; Pohlmann *et al.*, 2015). Key vehicles of cargo mRNAs are Rab5a-positive endosomes that shuttle along microtubules by the concerted action of plus-end directed kinesin-3 and minus-end directed cytoplasmic dynein (Baumann *et al.*, 2012). Important cargo mRNAs are, for example, all four septin mRNAs. Their local translation during transport is needed to form heteromeric septin complexes on the surface of transport endosomes. Endosomes deliver these

complexes to the hyphal tip forming a defined gradient of septin filaments at the growing pole (Baumann *et al.*, 2014; Olgeiser *et al.*, 2019; Zander *et al.*, 2016).

Rrm4 is the key RNA-binding protein of the transport process that recognises defined sets of cargo mRNAs via its three N-terminal RRMs (Fig. 1A; Olgeiser *et al.*, 2019). Rrm4 and bound cargo mRNAs are linked to endosomes by Upa1, containing a FYVE zinc finger for interaction with PI_3P lipids (phosphatidylinositol 3-phosphate; Fig 1A; Pohlmann *et al.*, 2015; Stenmark *et al.*, 2002). The adaptor protein contains a PAM2 motif (poly [A]-binding protein interacting motif 2; Albrecht & Lengauer, 2004; Jinek *et al.*, 2010; Kozlov *et al.*, 2004) and two PAM2 like (PAM2L) sequences. These motifs are crucial for interaction with MademoiseLLE (MLLE) domains of the poly(A)-binding protein Pab1 and Rrm4, respectively (Fig. 1A; Pohlmann *et al.*, 2015).

The MLLE domain was first identified as a conserved domain at the C-terminus of the human cytoplasmic poly(A)-binding protein 1 (PABP1C; Mangus *et al.*, 1998; Mangus *et al.*, 2003). Solution and crystal structures of PABC domains from PABP1C and ubiquitin ligase UBR5 showed that they are structurally conserved (Deo *et al.*, 2001; Kozlov *et al.*, 2001). The domain is about 70 amino acids in length and consists of five bundled α-helices. Interaction with the PAM2 binding motif (consensus sequence xxLNxxAxEFxP) is characterised by the central α-helix 3 with the sequence KITG<u>MLLE</u> and mediated by two adjacent hydrophobic pockets (Xie *et al.*, 2014), with the binding of the Phe residue of the PAM2 motif being the major determinant for this interaction (Kozlov & Gehring, 2010). Besides human PABPC1, there are currently only two additional proteins with MLLE domains described: the ubiquitin ligase UBR5 functioning, for example, during microRNA-mediated gene silencing (Su *et al.*, 2011) and Rrm4-type RNA-binding proteins from fungi (Fig. 1B; Müller *et al.*, 2019).

Mutations in the C-terminal MLLE domain of Rrm4 result in the loss of Rrm4 motility, suggesting that the link to endosomes is disrupted (Becht *et al.*, 2006). Consistently, the C-terminus of Rrm4 recognizes the PAM2L sequence of the adaptor protein Upa1 (Pohlmann *et al.*, 2015), suggesting that the interaction of MLLE domains with PAM2L sequences is responsible for its endosome association. In this study, we combine structural biology with fungal genetics to demonstrate that the C-terminal half of Rrm4 has three divergent MLLE domains with a flexible arrangement that contribute differentially to the endosomal attachment.

Results

Iterative structural modeling predicts three MLLE domains at the C-terminus of Rrm4

To generate structural models of the MLLE domains present in Rrm4, we focused on the C-terminal part of the protein (residues 421 to 792). This excluded the three N-terminal RRMs but included the previously predicted two C-terminal MLLE domains (Fig. 1A-B; Müller *et al.*, 2019). Subjecting this Rrm4 sequence region to iterative comparative modeling with TopModel (Fig. 1C; Mulnaes *et al.*, 2020a) revealed, as expected, the previously identified two regions with homology for MLLE domains located at residues 571-629 and 712-791 (denoted MLLE2 and MLLE3; Fig. 1C; Müller *et al.*, 2019). Unexpectedly, using the TopModel workflow with its efficient template selection capabilities (Mulnaes *et al.*, 2020a), we identified an additional *de novo* predicted MLLE domain located at residues 451-529 (denoted MLLE1; Fig. 1B-C; Fig. EV1A). Although the sequence identity between templates and their respective Rrm4 sequence stretches is only 17 to 32% (Fig. 1B, Fig. EV1A), the generated MLLE domain models have a high predicted local structural quality, as assessed by TopScore (Fig. 1C; Mulnaes & Gohlke, 2018). The generated models were also verified by the current deep neural network modeling approaches AlphaFold2 and RoseTTAFold (Fig. EV1B; Baek *et al.*, 2021; Jumper *et al.*, 2021), further indicating that the C-terminal half of Rrm4 has three MLLE domains instead of the previously identified two. All of these MLLE domains might be relevant for the interaction with Upa1.

X-ray analysis of the second MLLE domain confirms the predicted structural models

To verify the structural models further, we expressed and purified an N-terminally truncated version of the Rrm4 carrying the three MLLE domains in *Escherichia coli* (Fig. EV2A; version H-Rrm4-NT4 carrying an N-terminal hexa-histidine tag; Pohlmann *et al.*, 2015; Materials and methods). Size exclusion chromatography combined with multiangle light scattering (MALS) indicates that the protein is homogenous and does not form aggregates (Fig. EV2B-C). We thus set out to crystallize the protein for X-ray diffraction analysis (see Material and Methods). Testing 2016 different conditions, crystals were only obtained in individual cases after at least 7 days of incubation. A complete dataset was collected from a single crystal diffracting to 2.6 Å resolution and a $P4_32_12$ symmetry. Data and refinement statistics are given in Appendix Table S2. Surprisingly, the unit cell dimensions were small and, with a Matthews coefficient assuming 50% solvent content, only 128 amino acids would fit into the asymmetric unit of the crystal. Hence, the unit cell has an insufficient size to cover H-Rrm4-NT4, which contains 380 amino

112 acids. Using the predicted models of MLLE1-3 as templates for molecular replacement, only
113 MLLE2 gave a clear solution, showing after refinement that two copies of MLLE2 (residues
114 567-630) were present in the asymmetric unit. For comparison, previously, two copies of the
115 MLLE domain in the asymmetric unit were reported in crystals of MLLE of UBR5 (Munoz-
116 Escobar *et al.*, 2015). The structural data indicates that the protein was truncated from both
117 termini during crystallization, resulting in a shortened version of the H-Rrm4-NT4 protein that
118 formed stable crystals (see Material and methods). Both MLLE2^{Rrm4} copies adopt the same
119 overall fold (Fig. 2A) as seen by the RMSD of 0.29 Å over 59 C-alpha atoms. The MLLE2^{Rrm4}
120 crystal structure displays high similarity with the MLLE domain of the ubiquitin ligase UBR5
121 (MLLE^{UBR5}; Munoz-Escobar *et al.*, 2015; PDB code 3NTW, RMSD of 0.97 Å over 56 amino
122 acids) and the MLLE domain of PABPC1 (Kozlov *et al.*, 2010; PDB code 3KUS, RMSD of
123 1.34 Å over 61 amino acids). The MLLE2^{Rrm4} domain consists of four helices (designated α2 -
124 5; Fig. 2A) that are arranged as a right-handed superhelix similar to MLLE^{UBR5}. In comparison
125 to the MLLE domain of PABPC1, the first short helix is absent in both MLLE2^{Rrm4} and
126 MLLE^{UBR5} structures.

127 When comparing the obtained crystal structure with the MLLE2 ^{Rrm4} model generated by
128 TopModel, the average RMSD is 0.62 Å over the backbone atoms, close to the uncertainty of
129 the atomic coordinates of the experimental structure (Fig. 2B). Importantly, this confirms our
130 structural model of MLLE2^{Rrm4} and strongly suggests that the modeled MLLE1^{Rrm4} and
131 MLLE3^{Rrm4} domains should be of equally high quality.

132 We compared the models obtained of MLLE1-3^{Rrm4} with the known structure of the human
133 PABPC1 focusing on the well described PAM2 peptide binding pocket. This revealed that
134 MLLE3^{Rrm4} maintains a characteristic Gly residue at position 736 that binds the conserved Phe
135 residue of the PAM2 motifs, a major binding determinant in PABPC1 and UBR5 (Kozlov &
136 Gehring, 2010; Munoz-Escobar *et al.*, 2015; Fig. 2C). However, the binding interfaces of
137 MLLE1^{Rrm4} and MLLE2^{Rrm4} are altered compared to the 'canonical' binding site in PABPC1
138 and UBR5 (Fig. 2C). Instead of Gly, MLLE1^{Rrm4} and MLLE2^{Rrm4} have a Ser and Arg in the
139 corresponding positions 471 and 573. The notion that MLLE1^{Rrm4} and MLLE2^{Rrm4} may differ
140 from canonical MLLE domains is also supported by the lower sequence identity of MLLE1^{Rrm4}
141 and MLLE2^{Rrm4} when compared to previously characterized MLLE domains (Fig. EV1A). In
142 summary, structural modeling revealed the presence of three MLLE domains at the C-terminus
143 of Rrm4. Furthermore, the structure of the MLLE2^{Rrm4} domain was successfully verified by X-
144 ray crystallographic analysis. MLLE1^{Rrm4} and MLLE2^{Rrm4} are divergent in the key region of

145 PAM2 binding, suggesting that these domains might employ a different binding mode or show
146 a different binding specificity.

147 **The MLLE domains of Rrm4 form a binding platform with flexible arrangement of the**
148 **individual domains**

149 To study the relative arrangement of all three MLLE^{Rrm4} domains and the orientation to the N-
150 terminal RRMs, we performed Small-Angle X-ray Scattering (SAXS) experiments. We
151 expressed and purified H-Rrm4-NT4 as well as full-length protein with N-terminal GST fusion
152 (glutathione S-transferase; G-Rrm4) from *E. coli* (see Materials and methods). Primary data
153 analysis of the scattering curves (Tria *et al.*, 2015) revealed that both proteins are monomeric
154 and highly flexible in solution (Appendix Table S3; Fig. 2D-E; Fig. EV2D-E). To visualise the
155 different conformations, we performed an Ensemble Optimization Method (EOM) analysis for
156 both the G-Rrm4 and H-Rrm4-NT4 proteins (Fig 2D-E). We used our MLLE models and a
157 GST model (PDB entry: 1ua5) together with the protein sequence for G-Rrm4 as input, yielding
158 a distribution of different conformations of the protein in solution (representative models in Fig.
159 EV2E). One model of G-Rrm4, representing 25% of the population, revealed that the C-
160 terminal part containing MLLE1-3^{Rrm4} adopts an elongated and mainly unfolded but open
161 conformation (Fig. 2D; Fig. EV2D-E). The N-terminal part, containing RRM domains of the
162 GST fusion protein, adopts a more globular structure, indicating less flexibility within this
163 region (Fig. 2D; Fig. EV2D-E). Studying only the C-terminal part of Rrm4 revealed that the
164 most prominent model of this analysis (75 % of the population) has a nearly identical
165 conformation as the one selected for G-Rrm4 (Fig. 2D-E, Fig. EV2E). It suggests that the C-
166 terminal part of Rrm4-NT4 adopts a very similar orientation when expressed by itself. From
167 this analysis, one can deduce that the MLLE1-3^{Rrm4} domains form a C-terminal binding
168 platform with a flexible arrangement for multiple contact sites for binding partners. The RRM
169 domains and thus the RNA interaction site are clearly spatially separated from the protein
170 interaction platform.

171 **The third MLLE is essential for interaction with PAM2 like sequences of Upa1**

172 To evaluate the interaction capacity of MLLE1-3^{Rrm4}, we performed *in vitro* binding studies.
173 We expressed different deletion versions of Rrm4 as N-terminal GST fusions in *E. coli*. As a
174 control, we expressed an N-terminal GST fusion of the MLLE domain of Pab1 (Fig. 3A;
175 Materials and methods). To check the physical interaction with PAM2 and PAM2L sequences
176 of Upa1, we expressed 18 amino acid fragments (Fig. 3A, Fig. EV3B) as N-terminal hexa-
177 histidine-SUMO (HS) fusion proteins (see Materials and methods). In GST pull-down

178 experiments using GST fusion proteins as bait, G-Pab1-MLLE interacts with HS-PAM2 but
179 not with the HS-PAM2L motifs of Upa1 (Fig. EV3B, lane 2). Conversely, G-Rrm4-NT4
180 recognizes the two HS-PAM2L motifs of Upa1 but not the HS-PAM2 motif (Fig. EV3B, lane 3;
181 Pohlmann *et al.*, 2015). Interestingly, the interaction with both PAM2L motifs was lost when
182 MLLE3^{Rrm4} was deleted (G-Rrm4-NT4-M3Δ; Fig. EV3B, lane 6), while constructs with
183 deletion of MLLE1^{Rrm4} or MLLE2^{Rrm4}, or MLLE1^{Rrm4} and MLLE2^{Rrm4}, still interacted with the
184 HS-PAM2L motifs of Upa1 (Fig. EV3B, lane 4,5 and 7).

185 To obtain quantitative data on the protein/peptide interactions, we performed isothermal
186 titration calorimetry (ITC) experiments with purified proteins (Fig. EV3C) using synthetic
187 peptides with a length of 18 amino acids (PAM2^{Upa1}, PAM2L1^{Upa1}, and PAM2L2^{Upa1}; Fig. 3A).
188 From the curves, the binding constant K_D and the binding stoichiometry was calculated, which
189 in all cases indicated a 1:1 ratio between the G-Rrm4-NT4 protein and the binding partner.

190 Testing G-Pab1-MLLE with the peptides revealed a K_D of 14.6 µM for PAM2^{Upa1} (Fig.
191 EV3D), which is within the range of observed K_D of 0.2 to 40 µM for known MLLE/PAM2
192 interactions like the MLLE domain of PABPC1 with various PAM2 sequences (Mattijssen *et*
193 *al.*, 2021). Testing G-Pab1-MLLE with PAM2L1^{Upa1} and PAM2L2^{Upa1} peptides, no indication
194 for binding was observed. PAM2L sequences are rich in acidic residues and exhibit a different
195 FxxP spacing than the canonical FXP sequence of PAM2 sequences in the core region (Fig.
196 3A, EV3D; see Discussion). The observed binding behaviour indicates a clear binding
197 specificity differentiating PAM2 and PAM2L peptides. This is in line with the previously
198 published GST pull-down experiments (Pohlmann *et al.*, 2015).

199 In comparison, testing G-Rrm4-NT4 with the peptides revealed a K_D of 14.9 µM for
200 PAM2L1^{Upa1} and 5.1 µM for PAM2L2^{Upa1} and no binding to PAM2^{Upa1} (Fig. 3B). This suggests
201 a similar affinity when compared to the interactions of MLLE^{Pab1} with PAM2 and demonstrates
202 the high sequence specificity of the MLLE domains to their respective PAM2L sequences (see
203 Discussion).

204 Analysing G-Rrm4-NT4-M3Δ with a deletion of MLLE3^{Rrm4} revealed that binding to
205 PAM2L1^{Upa1} and PAM2L2^{Upa1} was no longer detectable (Fig. 3C). This is in line with
206 observations from the GST pull-down experiments (Fig. EV3B). This suggests that MLLE3^{Rrm4}
207 is essential for binding. Testing G-Rrm4-NT4 versions carrying deletions in MLLE1^{Rrm4} and
208 MLLE2^{Rrm4} revealed no difference in binding affinity (Fig. EV3E-F). Even testing G-Rrm4-
209 NT4 with both MLLE domains deleted revealed a binding affinity in the same range as the
210 wildtype version containing all three MLLEs (Fig. 3D). We conclude that (i) MLLE3^{Rrm4} is
211 vital for recognizing PAM2L sequences with a higher affinity to PAM2L2 and (ii) neither

212 MLLE1^{Rrm4} nor MLLE2^{Rrm4} contribute to the binding of PAM2L or PAM2 motifs. This is
213 consistent with our structural analysis revealing a differences in the binding site for these MLLE
214 domains (see Discussion).
215

216 **The third MLLE domain of Rrm4 is essential for its function**

217 To address how the different MLLE domains contribute to the biological function of Rrm4, we
218 generated *U. maydis* strains carrying deletions in the respective domains of Rrm4 (Fig. 4A). As
219 genetic background, we used laboratory strain AB33, expressing the heteromeric master
220 transcription factor of hyphal growth (bE/bW) under control of the nitrate inducible promoter
221 P_{nar1}. Thereby, polar hyphal growth can be elicited efficiently and in a highly reproducible
222 fashion by changing the nitrogen source (Fig. 4B, top; Brachmann *et al.*, 2001). To investigate
223 dynamic endosomal transport, we used strains expressing functional C-terminal fusion Upa1-
224 Gfp and Rrm4-Kat (fusion with enhanced version of the green fluorescent protein, Clontech,
225 and monomeric version of red fluorescent protein mKate2, respectively; Müntjes *et al.*, 2020;
226 Pohlmann *et al.*, 2015; see Materials and methods).
227 The resulting hyphae grew with a defined axis of polarity, i.e., they expanded at the hyphal
228 tip and inserted basal septa leading to the formation of empty sections (Fig. 4B-C). Loss of
229 Rrm4 (*rrm4Δ* strain) caused the formation of hyphae growing at both ends, characteristic for
230 aberrant bipolar growth (Fig. 4B-C; Pohlmann *et al.*, 2015). Testing Rrm4-Kat versions
231 carrying deletions of MLLE1^{Rrm4} or MLLE2^{Rrm4} did not cause alterations in unipolar growth
232 (Fig. 4B-C). Furthermore, endosomal shuttling and co-localisation were indistinguishable from
233 wildtype (Fig. 4D-E). Also, the number of Rrm4-Kat-positive endosomes (number of signals /
234 10 µm, Fig. EV4A), velocity, and processivity (Fig. EV4B-C) were comparable to wildtype.
235 Hence, the first two MLLE domains were dispensable for polar growth and endosomal shuttling
236 under optimal growth conditions. Since the deletion of the first two MLLEs did not substantially
237 alter the function of Rrm4, we can infer that the deletion neither affects the overall structure of
238 the protein nor interfere with other domains like the RNA-binding domain of the protein. This
239 supports the conclusions of our biochemical experiments (see above).
240 Importantly, testing strains expressing Rrm4-Kat with deletion of the third MLLE domain
241 revealed a loss-of-function phenotype similar to *rrm4Δ* strains. The amount of bipolar hyphae
242 was comparable to *rrm4Δ* strains (Fig. 4B-C; Becht *et al.*, 2006). We observed drastic alteration
243 in shuttling, and Rrm4 aggregates did not co-localise with motile Upa1-positive signals (Fig.
244 4D-E). While the Rrm4 signals were static (Fig. 4D-E; Fig. EV4A-C) the amount of motile

245 Upa1-Gfp positive endosomes, their velocity, and their processivity were not affected (Fig.
246 EV4A-C, summarised in Fig. EV4D). This is consistent with previous results showing that the
247 third MLLE domain is important for the movement of Rrm4 and that endosomal shuttling of
248 Upa1 is not affected if Rrm4 is missing (Baumann *et al.*, 2012; Becht *et al.*, 2006). To conclude,
249 MLLE3^{Rrm4} is an essential domain for Rrm4 attachment to endosomes in contrast to MLLE1
250 and MLLE2^{Rrm4}.
251

252 **The second MLLE domain plays accessory roles in endosomal Rrm4 attachment**

253 To investigate the biological role of MLLE1^{Rrm4} and MLLE2^{Rrm4} in more detail, we generated
254 strains expressing Rrm4-M12Δ-Kat, lacking MLLE1^{Rrm4} and MLLE2^{Rrm4} domains, and tested
255 the influence on hyphal growth. Unipolar growth was not disturbed (Fig. 5A-B). To challenge
256 endosomal attachment of Rrm4, we expressed Upa1-Gfp versions carrying mutations in
257 PAM2L motif 1 or 2 as well as in both motifs; these motifs are important for Rrm4 interaction
258 (Fig. 4A; Pohlmann *et al.*, 2015). Strains expressing Rrm4-M12Δ-Kat in combination with
259 mutated PAM2L1 or PAM2L2 of Upa1 showed unipolar growth comparable to wildtype (Fig.
260 5A-B), indicating that MLLE1^{Rrm4} and MLLE2^{Rrm4} are dispensable for unipolar growth even
261 when the endosomal attachment was weakened by expressing Upa1 versions with mutated
262 PAM2L motifs (Fig. EV4D). When studying Upa1 mutated in both PAM2L motifs, we
263 observed an aberrant bipolar growth phenotype comparable to the *upa1Δ* strain (Fig. 5A-B).
264 This was expected, since the interaction of Rrm4 to endosomes is mediated by both PAM2L
265 motifs (Pohlmann *et al.*, 2015). Analysing Rrm4-M12Δ-Kat in this genetic background
266 revealed no additive phenotype (Fig. 5A-B). This reinforces that the interactions of PAM2L
267 motifs of Upa1 are the major determinants for endosomal attachment of Rrm4.
268 Next, we investigated endosomal shuttling. In strains expressing Rrm4-M12Δ-Kat missing
269 MLLE1^{Rrm4} and MLLE2^{Rrm4} endosomal shuttling was not disturbed (Fig. 5C). The amount of
270 motile Rrm4-M12Δ-Kat positive signals, their velocity, and their processivity were not affected
271 (Fig. EV5A). Like above, we challenged endosomal attachment of Rrm4 by expressing Upa1
272 versions with mutations in the PAM2L motifs. As expected, simultaneous mutation of both
273 PAM2L motifs of Upa1 resulted in a reduction in the number of Rrm4-Kat positive shuttling
274 endosomes (Fig. 5C, EV5E; Pohlmann *et al.*, 2015). In about 80% of hyphae, Rrm4-Kat found
275 to be aberrantly attached to microtubules (MT) when both PAM2L motifs are mutated (Fig.
276 5C-D). This is a characteristic feature for altered endosomal attachment of Rrm4 due to the

277 static accumulation of Rrm4-Kat, which can be also seen in *upa1Δ* strains (Fig. EV5C;
278 Jankowski *et al.*, 2019).

279 To analyse the influence of individual PAM2L motifs we determined the amount of hyphae
280 with aberrant microtubule staining in strains co-expressing Rrm4-Kat and an Upa1-Gfp version
281 with mutations of PAM2L sequence 1 or 2 (Fig. 5D). Mutations in PAM2L1 and PAM2L2
282 causes 8% and 19% of hyphae with aberrant MT staining, respectively. This indicates that the
283 interaction of PAM2L2 is more important for correct endosomal attachment of Rrm4. This is
284 consistent with our biochemical results demonstrating that MLLE3^{Rrm4} binds stronger to
285 PAM2L2 of Upa1 than to PAM2L1 (Fig. 3D).

286 Next, we investigated the association of Rrm4-M12Δ-Kat in strains expressing Upa1-
287 PAM2L1. Thus, the endosomal attachment was solely dependent on the interaction of
288 MLLE3^{Rrm4} with the PAM2L2 sequence of Upa1. We did observe 6% of hyphae with aberrant
289 MT staining (Fig. 5D; Fig. EV4D). This was comparable to strains expressing Rrm4-Kat
290 suggesting no clear difference (Fig. 5D). However, testing Upa1 with its PAM2L2 mutated,
291 leaving only PAM2L1 for interaction with Rrm4, we observed a clear increase in hyphae with
292 aberrant MT staining when comparing strains co-expressing Rrm4-M12Δ-Kat versus Rrm4-
293 Kat (52% versus 19%; Fig. 5D-E). Hence, the region covering MLLE1^{Rrm4} and MLLE2^{Rrm4} was
294 important for Rrm4 attachment. Finally, we tested individual deletions in MLLE1^{Rrm4} and
295 MLLE2^{Rrm4} in combination with mutated PAM2L2 in Upa1 to dissect the role of the different
296 MLLE domains. In the strains expressing Rrm4-Kat or Rrm4-M1Δ-Kat, the amount of hyphae
297 with aberrant MT staining was comparable (18% versus 11%, respectively; Fig. 5D). However,
298 strains expressing Rrm4-M2Δ-Kat exhibited an increased amount of hyphae with aberrant MT
299 staining that was comparable to Rrm4-M12Δ-kat (51% versus 52% respectively; Fig. 5D; Fig.
300 EV4D). To conclude, for MLLE1^{Rrm4} we were unable to assign a clear function yet. However,
301 MLLE2^{Rrm4} plays an accessory role in the endosomal attachment of Rrm4. In essence, the C-
302 terminus of Rrm4 contains three MLLE domains, with MLLE2^{Rrm4} fulfilling an accessory role
303 and MLLE3 having an essential function during the attachment of mRNPs to endosomes.

304 **Discussion**

305 Combining structural biology and biophysical techniques with fungal genetics and cell biology,
306 we addressed how mRNPs can be mechanistically linked to endosomes in the model fungus *U.*
307 *maydis*. Previously, it was found that the C-terminal MLLE domain of Rrm4 is needed for
308 shuttling (Becht *et al.*, 2006) and that the C-terminus of Rrm4 interacts with two PAM2L motifs
309 of Upa1 (Pohlmann *et al.*, 2015). Now, we demonstrate that the C-terminus of Rrm4 contains
310 not only two MLLE domains, but a sophisticated binding platform consisting of three MLLE

311 domains that collaborate for optimal functionality in linking the key RNA transporter to
312 endosomes. We disclose a strict hierarchy with main and accessory domain. The accessory
313 MLLE2 domain shows variations in the critical region of the predicted PAM2 binding pocket,
314 suggesting a novel mode of interaction with currently unknown interaction partners. To the best
315 of our knowledge, Rrm4 represents the first protein containing multiple MLLE domains to form
316 a binding platform. This interaction unit is essential for correct endosomal attachment and,
317 hence, mRNP trafficking.

318 **The MLLE / PAM2 connection**

319 The founding member of the MLLE domain family is present at the C-terminus of the poly(A)-
320 binding protein PABPC1. This domain interacts with PAM2 motifs of numerous interaction
321 partners such as GW182, eRF3, and the RNA-binding protein LARP4 functioning in
322 microRNA biology, translational termination, and posttranscriptional control, respectively
323 (Jinek *et al.*, 2010; Kozlov & Gehring, 2010; Yang *et al.*, 2011). Structural analysis revealed a
324 common mode of binding, where the Leu and particularly the Phe of the PAM2 consensus motif
325 xxLNxxAxEFxP (Fig. EV3A) are interacting with helix 2 and 3 as well as helix 3 and 5 of
326 MLLE domain, respectively (Kozlov & Gehring, 2010; Xie *et al.*, 2014). Indeed, the interaction
327 of MLLE with a hydrophobic amino acid is highly conserved, which in most cases is Phe with
328 a known exception in the variant PAM2w motif of LARP4 and LARP4A, where Trp is found
329 (Fig. EV3A; Grimm *et al.*, 2020; Yang *et al.*, 2011; Xie *et al.*, 2014).
330 Studying the MLLE domain-containing protein Rrm4, we discover that the protein has
331 three MLLE domains in its C-terminal half. $MLLE3^{Rrm4}$ binds PAM2L motifs of Upa1 with a
332 K_D of 5 and 15 µM for $PAM2L2^{Upa1}$ and -1, respectively. The binding affinities are in the same
333 range as described for other MLLE/PAM2 interactions: for example, the binding of
334 $MLLE^{PABPC1}$ with $PAM2^{LARP1}$, $PAM2^{Tob2-125}$, $PAM2^{LARP4}$ exhibit a K_D of 3.8, 16 and 22 µM,
335 respectively (Mattijssen *et al.*, 2021). Importantly, our biophysical assessment confirms the
336 exquisite binding specificity of $MLLE^{Rrm4}$ that recognizes $PAM2L1^{Upa1}$ and -2 but not
337 $PAM2^{Upa1}$ version. PAM2L sequences contain a stretch of acidic amino acids in the N-terminal
338 half, and the spacing of FxxP in the core sequence is altered (Fig. EV3A). These variations
339 might account for the differential binding mode. Visual inspection of the potential PAM2L
340 binding region in the predicted model revealed that $MLLE3^{Rrm4}$ contains a Gly at position 736
341 to sustain the binding of an aromatic residue of PAM2L as described for other MLLE domains
342 (see above). However, we were unable to uncover the structural basis for the sequence

343 specificity. Towards this end, future structural studies are required to provide detailed
344 information on the interaction of MLLE3^{Rrm4} with PAM2L sequences.
345 Differential PAM2 binding has also been described for the MLLE^{UBR5}. This MLLE domain
346 interacts with PAM2^{PAIP} with an affinity of 3.4 µM (Lim *et al.*, 2006), whereas it binds a
347 PAM2L sequence (Fig. EV3A) in its own HECT domain with lower affinity (K_D of 50 µM).
348 The latter interaction has been implicated in the regulation of the HECT ligase activity (Munoz-
349 Escobar *et al.*, 2015). Interestingly, the PAM2L sequence within the HECT domain of UBR5
350 is highly similar to the PAM2L1 and -2 of Rrm4: (i) the sequences contain an acidic stretch N-
351 terminal to the conserved Phe (Fig. EV3A), (ii) the distance between Phe and Pro is two instead
352 of one amino acid, and (iii) the PAM2L sequence contains an additional bulky Tyr in close
353 vicinity to the Phe residue. Remarkably, MLLE^{PABC1} does not recognise the PAM2L sequence
354 of UBR5 (Munoz-Escobar *et al.*, 2015). In essence, although the strong sequence specificity of
355 MLLE^{Rrm4} and MLLE^{Pab1} from *U. maydis* is, to the best of our knowledge, so far unique, we
356 hypothesise that differential PAM2 and PAM2L interactions are evolutionarily conserved and
357 might be more widespread than currently anticipated.
358 We observed also clear binding specificity for MLLE^{Pab1} from *U. maydis* that interacts with
359 PAM2^{Upa1} but not the PAM2L sequences from Upa1 (Fig. 6). MLLE^{Pab1} binds with comparable
360 affinity to the PAM2^{Upa1} (K_D of about 14 µM, Fig EV3D). Previously, we showed that mutations
361 in PAM2^{Upa1} strongly decreased MLLE^{Pab1} binding but did not interfere with the endosomal
362 shuttling of Pab1 (Pohlmann *et al.*, 2015). Thus, there might be other members of the endosomal
363 mRNPs interacting with Pab1 and stabilising its endosomal association. In fact, the dimerising
364 scaffold protein Upa2 of endosomal mRNA transport contains four PAM2 motifs offering eight
365 potential PAM2 motifs for interaction with Pab1 (Fig. 6). However, mutating all four PAM2
366 motifs did not interfere with endosomal mRNA transport, although interaction with MLLE^{Pab1}
367 was lost (Jankowski *et al.*, 2019), confirming a potential redundancy. Consistently, mutations
368 in PAM2 of human LARP4B did not interfere with the function of stress granule recruitment,
369 also suggesting in this case the presence of additional factors (Grimm *et al.*, 2020).
370 Studying the other two MLLE domains of Rrm4 revealed that both lack the canonical Gly
371 for interactions with PAM2 or PAM2L sequences. MLLE1^{Rrm4} and MLLE2^{Rrm4} have Ser471
372 and Arg573 instead, respectively. Consistently, MLLE1^{Rrm4} and MLLE2^{Rrm4} do not bind PAM2
373 or PAM2L sequences. Thus, although the general fold of the MLLE domain is probably
374 conserved in MLLE1^{Rrm4} and MLLE2^{Rrm4}, these domains most likely exhibit a different binding
375 specificity to their potential protein partner. Our detailed *in vivo* analysis revealed that MLLE2
376 carries out an accessory function for the correct attachment of Rrm4 during endosomal

377 shuttling. In case of MLLE1 we did not identify a clear function so far. However, we believe
378 that all three MLLE domains are functional important. This is supported by the fact that the
379 presence of a MLLE binding platform with three MLLE domains is evolutionarily conserved.
380 Even Rrm4 versions of the distantly related fungus *Rhizophagus irregularis* contains three
381 MLLE domains (Mucoromycota, determined by AlphaFold; Müller *et al.*, 2019).
382 Studying the spatial arrangement of the three MLLE domains revealed that they form a
383 highly flexible binding platform. This would allow for the simultaneous interaction of several
384 binding partners and potential rearrangements like an induced fit after binding. Such a scenario
385 might be particularly important during the loading and unloading of mRNPs to endosomes.
386 Noteworthy, the N-terminal RNA-binding domain consisting of three RRMs is clearly
387 separated from the MLLE domains for endosomal attachment. This is comparable with the
388 arrangement of RRM and MLLE domains in human PABPC1: the four N-terminal RRM
389 domains interact with the poly(A) tail of mRNAs, and the MLLE domain is exposed by a
390 flexible spacer region for protein/protein interactions (Schäfer *et al.*, 2019). Within the spacer
391 region, additional interactions with the RRM2 of PABPC1 were found, suggesting a function
392 in multimerization of the protein on the poly(A) tail of mRNAs (Sawazaki *et al.*, 2018).

393 **Conclusion**

394 Endosomal mRNA transport is evolutionarily highly conserved. Besides hyphal growth in
395 fungi, it is important for endosperm development in plants as well as neuronal functions in
396 animals and humans (Béthune *et al.*, 2019; Fernandopulle *et al.*, 2021; Müntjes *et al.*, 2021;
397 Tian *et al.*, 2020a). Malfunction causes defects in polar growth in fungi and has been implicated
398 in neuronal diseases such as Charcot-Marie-Tooth type 2B neuropathy or amyotrophic lateral
399 sclerosis in humans (Cioni *et al.*, 2019; Liao *et al.*, 2019).
400 A key question is how mRNPs are linked to endosomes. In plants, two RRM-type RNA-binding
401 proteins form a complex with cargo mRNAs and the endosomal component *N*-ethylmaleimide-
402 sensitive factor NSF as well as Rab5a (Tian *et al.*, 2018; Tian *et al.*, 2020a; Tian *et al.*, 2020b).
403 Comparably, the FERRY complex (Five-subunit Endosomal Rab5 and RNA/ribosome
404 intermediarY) interacts with the activated GTP-bound form of Rab5 during endosomal mRNA
405 transport in neurons (Schuhmacher *et al.*, 2021; Quentin *et al.*, 2021). Further examples are the
406 membrane-associated protein Annexin 11 that functions in linking large RNA granules to
407 lysosomal vesicles during mRNA transport in axons and dendrites (Liao *et al.*, 2019). Thus, a
408 number of components and interactions are known, however detailed structural insights are
409 scarce. Here, we demonstrate that in hyphae, endosomal attachment of Rrm4 is mediated by an

410 MLLE binding platform with a non-canonical accessory domain joining an essential MLLE
411 domain for perfect interaction to Upa1 on the endosomal surface (Fig. 6). This binary
412 interaction in the core of the transport mRNPs is supported by numerous interactions of
413 additional protein partners such as Upa2 and Pab1 that assist in the attachment of components
414 to the endosomal surfaces (Fig. 6). In essence, studying endosomal mRNP transport in fungal
415 model systems might guide future research endeavours in plant and neuronal systems.
416

417 **Materials and methods**

418 **Structural modeling of C-terminal MLLE domains of Rrm4**

419 To obtain structural models of the C-terminal region of Rrm4, an iterative homology modeling
420 approach was used with the TopModel workflow (Mulnaes *et al.*, 2020a). Initially, the complete
421 C-terminal region (421 to 792) was submitted as input in TopModel and identified templates
422 for MLLE3^{Rrm4} (665 – 792 AA; Fig. 1C, Fig. EV1A). Then, the rest of the C-terminal part
423 comprising amino acids 421 to 664 was resubmitted as input and identified other templates as
424 a new starting point for the MLLE2^{Rrm4} (571-629). Likewise, the remaining C-terminal
425 sequence comprising amino acids 421 to 549 was resubmitted as input, which identified other
426 templates as a new starting point for the MLLE1^{Rrm4} (446-530). In total, this led to the
427 identification of three MLLE domains, for which structural models were generated using
428 default TopModel parameters. The quality of the structural models was assessed with TopScore
429 (Mulnaes & Gohlke, 2018).

430 **Plasmids, strains, and growth conditions**

431 For molecular cloning of plasmids, *Escherichia coli* Top10 cells (Thermofisher C404010) and
432 for recombinant protein expression *E.coli Lobstr* cells (Kerafast EC1002) were used
433 respectively. Sequence encoding H-Rrm4-NT4 was subcloned into pET22 vector (Merck
434 69744) with an N-terminal hexa-histidine tag for crystallization studies. Sequence encoding
435 MLLE variants were inserted into pGEX-2T vector (Merck GE28-9546-53) containing GST
436 sequence in N-terminus for pulldown and ITC experiments. Sequence encoding PAM2 variants
437 were inserted into Champion pET-Sumo vector (Thermofisher K30001). pRarepLys plasmid
438 was co-transformed in *E. coli Lobstr strain* to supplement the rare codons for efficient
439 recombinant protein production. *E. coli* transformation, cultivation, and plasmid isolation were
440 conducted using standard techniques. All *U. maydis* strains are derivatives of AB33, in which
441 hyphal growth can be induced by switching the nitrogen source in the medium (Brachmann *et*
442 *al.*, 2001). *U. maydis* yeast cells were incubated in complete medium (CM) supplemented with
443 1% glucose, whereas hyphal growth was induced by changing to nitrate minimal medium (NM)
444 supplemented with 1% glucose, both at 28°C (Brachmann *et al.*, 2001). Detailed growth
445 conditions and general cloning strategies for *U. maydis* are described elsewhere (Baumann *et*
446 *al.*, 2012; Brachmann *et al.*, 2004; Terfrüchte *et al.*, 2014). All plasmids were verified by
447 sequencing. Strains were generated by transforming progenitor strains with linearized plasmids.
448 Successful integration of constructs was verified by diagnostic PCR and by Southern blot

449 analysis (Brachmann *et al.*, 2004). For ectopic integration, plasmids were linearized with *Ssp*I
450 and targeted to the *ip*^{S} locus (Loubradou *et al.*, 2001). A detailed description of all plasmids,
451 strains, and oligonucleotides is given in Appendix Tables S3–S7. Sequences are available upon
452 request.

453 **Recombinant protein expression and purification**

454 *E. coli* cells from freshly transformed plates were inoculated in 20 ml expression media. In
455 order to produce high density expression cultures with tight regulation of induction and
456 expression in shake flasks we designed a complex media inspired from the principle of Studier's
457 autoinduction media (Studier, 2005). We use adequate amount of glucose to prevent the
458 unintended induction and leaky expression of target protein as well as phosphate buffer to
459 prevent acidity as a result of glucose metabolism from the excessive glucose in the media. In
460 addition, the medium contained glycerol, nitrogen, sulphur, and magnesium for promoting high
461 density growth. Unlike the studier's autoinduction media our media lack lactose therefore
462 expression can be induced with IPTG and expressed at required temperature (Studier, 2005; 1.6
463 % Trypton, 1% Yeast extract, 50 mM Na_2HPO_4, 50 mM KH_2PO_4, 25 mM $[NH_4]_2SO_4$, 0.5%
464 Glycerol, 0.5% Glucose, 2 mM $MgSO_4$) with ampicillin (100 mg/ml) and chloramphenicol (34
465 mg/ml) or kanamycin (200 mg/ml) and chloramphenicol (34 mg/ml) and grown overnight (16
466 hours) at 37 °C, 200 rpm. Note, high concentration of kanamycin was used to prevent the
467 unintended resistance promoted by high phosphate concentration (Studier, 2005). Supernatant
468 from the overnight culture was removed by centrifugation at 4 °C, 5000 g for 2 minutes. Cells
469 were resuspended in fresh media with a starting OD_{600} of 0.1 and grown at 37 °C, 200 rpm for
470 about 2 hours 30 minutes until the OD_{600} = 1. Protein expression was induced at 28 °C, 200
471 rpm, for 4 hours by addition of 1 mM IPTG, and harvested by centrifugation at 4°C, 6,000 g
472 for 5 minutes. Protein purification was performed as per the previous report (Abts *et al.*, 2013).
473 Hexa-histidine tagged protein was purified using Nickle-based affinity chromatography
474 (HisTrap HP GE healthcare) on Akta prime FPLC system. Cells were thawed on ice and
475 resuspended in buffer A (20 mM HEPES pH 8.0, 200 mM NaCl, 1 mM EDTA, 10 mM
476 Imidazole pH 8.0; 1 mM PMSF, 0.5 mg/ml Lysozyme, 0.5 mg/ml DNase, 1mM β
477 mercaptoethanol [β-ME]). Subsequently, cells were lysed by sonication on ice and centrifuged
478 at 4 °C 18,000 g for 30 minutes. Resulting supernatant was loaded on to a pre-equilibrated
479 column with buffer B (20 mM HEPES pH 8.0, 200 mM NaCl,10 mM Imidazole), washed with
480 buffer C (20 mM HEPES pH 8.0, 200 mM NaCl, 50 mM Imidazole, 1 mM β-ME), eluted with
481 buffer D (20 mM HEPES pH 8.0, 200 mM NaCl, 300 mM Imidazole, 1mM β-ME) and further

482 purified by Size Exclusion Chromatography (HiLoad 26/600 Superdex 200, GE healthcare),
483 pre-equilibrated with buffer E (20 mM HEPES pH 8.0, 200 mM NaCl, 1 mM β-ME). For
484 crystallization studies, H-Rrm4-NT4 was purified as above except that the buffers were
485 prepared with high salt (500 mM NaCl) and without β-ME.
486 GST-tagged protein was purified using Glutathione-based affinity chromatography (GSTrap
487 FF GE healthcare). Cells were thawed on ice and resuspend in Buffer F (20 mM HEPES pH
488 8.0, 200 mM NaCl, 1 mM EDTA, pH 8.0; 1 mM PMSF, 0.1 mg/ml Lysozyme, 1 mM β-ME).
489 Subsequently, cells were lysed by sonication on ice and centrifuged at 4 °C, 18,000 g for 30
490 minutes. The resulting supernatant was loaded onto a pre-equilibrated column with buffer E (20
491 mM HEPES pH 8.0, 200 mM NaCl, 1 mM β-ME) and washed with the same buffer, eluted
492 with buffer H (20 mM HEPES pH 8.0, 200 mM NaCl, 10 mM reduced glutathione, 1 mM β-
493 ME), and further purified by size exclusion chromatography (HiLoad 16/600 Superdex 200 GE
494 healthcare), pre-equilibrated with buffer E. Protein purity was analysed on SDS PAGE. All the
495 purified proteins were concentrated, centrifuged at 4°C, 100,000 g for 30 minutes, quantified
496 by Nanodrop A280, aliquoted, and stored at -80°C. Peptides for ITC experiments were custom-
497 synthesised and purchased from Genscript, USA (see Fig. 3A for peptide sequence).

498 **GST pull-down experiments**

499 Pull-down assays were performed as per the previous report (Jankowski *et al.*, 2019). GST-
500 MLLE variants and HS-PAM2 variants were expressed in *E. coli* and harvested as described
501 above. Cell pellets from 50 ml *E. coli* expression culture were resuspended in 10 ml buffer F
502 (20 mM HEPES pH 8.0, 200 mM NaCl, 1 mM EDTA; 0.5% Nonidet P-40, 1 mM PMSF, 0.1
503 mg/ml Lysozyme). Cells were lysed by sonication on ice and centrifuged at 4 °C, 16,000 g for
504 10 minutes. 1 mL of the resulting supernatant was incubated for 1 hour at 4°C on constant
505 agitation of 1,000 rpm with 100 µL glutathione sepharose (GS) resin (GE healthcare), pre-
506 equilibrated in buffer F. The GS resin was washed three times with 1 ml of buffer G (20 mM
507 HEPES pH 8.0, 200 mM NaCl, 1 mM EDTA, 0.5 % Nonidet P-40). Subsequently, supernatant
508 of HS-PAM2 variants was added to the GST-MLLE variant bound resins and incubated for 1
509 hour at 4 °C on agitation. The resins were washed as aforementioned and resuspended in 100
510 µL of 2x Laemmli loading buffer and boiled for 10 minutes at 95 °C and analysed by western
511 blotting.

512 **SDS-PAGE and immunoblotting**

513 All SDS–PAGE and Western blotting experiments were performed as per the previous report.
514 (Jankowski *et al.*, 2019). For Western blotting, protein samples were resolved by 12 % SDS–
515 PAGE and transferred to a PVDF membrane (GE Healthcare) by semi-dry blotting. Western
516 blot analysis was performed with anti-His (Sigma H1029). Anti-mouse IgG HRP conjugate
517 (Promega W4021) was used as a secondary antibody. The activity was detected using the
518 AceGlow blotting detection system (VWR Peqlab, Erlangen, Germany).

519 **Multiangle laser light scattering (MALS)**

520 MALS was performed as per the previous report (Weiler *et al.*, 2021). Superdex 200 Increase
521 10/300 GL column (GE Healthcare) was pre-equilibrated overnight at a flow rate of
522 0.1 ml/minute with buffer E (20 mM HEPES pH 8.0, 200 mM NaCl, 1 mM β-ME). For each
523 analysis, 200 µl of protein sample at the concentrations of 2.0 mg/ml was loaded onto the
524 column at the flow rate of 0.6 ml/minute using 1260 binary pump (Agilent Technologies).
525 Scattered light was measured with miniDAWN TREOS II light scatterer, (Wyatt Technologies),
526 and the refractive index was measured with Optilab T-rEX refractometer, (Wyatt
527 Technologies). Data analysis was performed with the software ASTRA 7.3.2.21 (Wyatt
528 Technologies; Slotboom *et al.*, 2008).

529 **Crystallization of H-Rrm4 NT4**

530 Initial crystallization conditions were searched using MRC 3 96-well sitting drop plates and
531 various commercially available crystallization screens at 12 °C. 0.1 µl homogeneous protein
532 solution (10 mg/ml in 20 mM Hepes pH 8.0, 500 mM NaCl) was mixed with 0.1 µl reservoir
533 solution and equilibrated against 40 µl of the reservoir. After one week, initial rod-shaped
534 crystals were found, which were then further optimized by slightly varying the precipitant
535 concentrations. Optimisation was also performed in sitting drop plates (24-well) at 12 °C but
536 by mixing 1 µl protein solution with 1 µl of the reservoir solution, equilibrated against 300 µl
537 reservoir solution. Best diffracting crystals were grown within 7 days in 0.1 M Hepes pH 7.5,
538 20% (w/v) PEG 10000 (Qiagen PEG I, D5). Crystal-containing drops were overlaid with 2 µl
539 mineral oil before harvesting the crystal and immediately flash-frozen in liquid nitrogen.

540 **Data collection, processing, and structure refinement**

541 A complete data set of the H-Rrm4-NT4 were collected at beamline ID23EH1 (ESRF, France)
542 at 100 K and wavelength 0.98 Å up to 2.6 Å resolution. All data were processed using the

automated pipeline at the EMBL HAMBURG and reprocessed afterwards using XDS (Kabsch, 2014). The above obtained model for MLLE2 by TopModel was successfully used to phase the 2.6 Å data set of Rrm4 MLLE using the program Phaser from the program suite Phenix (Afonine *et al.*, 2012). The structure was then refined in iterative cycles of manual building and refinement in coot (Emsley & Cowtan, 2004) followed by software-based refinements using the program suite Phenix (Afonine *et al.*, 2012.) All residues were in the preferred and additionally allowed regions of the Ramachandran plot (Appendix Table S2). The data collection and refinement statistics are listed in Appendix Table S2. The comparison of the structure and models were performed using the superpose tool of PHENIX calculating the corresponding RMSD. The images of the models were prepared using PyMOL. The structure was deposited at the worldwide protein data bank under the accession code 7PZE.

Small angle X-ray scattering

We collected all SAXS data on beamline BM29 at the ESRF Grenoble (Franke *et al.*, 2017 Pernot *et al.*, 2013; Pernot *et al.*, 2010). The beamline was equipped with a PILATUS 2M detector (Dectris) with a fixed sample to distance of 2.827 m. To prevent concentration-dependent oligomerization, we performed the measurements with concentrations of 0.6 mg/ml at a temperature of 10 °C in buffer E. We collected one frame each second and scaled the data to absolute intensity against water. All used programs for data processing were part of the ATSAS Software package (Version 3.0.3;Manalastas-Cantos *et al.*, 2021). The primary data reduction was performed with the program Primus (Konarev *et al.*, 2003). With Primus and the included Guinier approximation (Franke & Svergun, 2009), we determined the forward scattering *I(0)* and the radius of gyration (R_g). The pair-distribution function *p(r)* was calculated with Gnom (Svergun, 1992) and was used to estimate the maximum particle dimension (D_{max}). Due to the high flexibility of the proteins we performed an Ensemble Optimization Method (EOM; Tria *et al.*, 2015; default parameters, 10,000 models in initial ensemble, native-like models, constant subtraction allowed) with the predicted MLLE domains from TopModel (Mulnaes *et al.*, 2021; Mulnaes *et al.*, 2020b) for H-Rrm4-NT4 and G-Rrm4 with an additional GST (PDB1ua5). We uploaded the data to the Small Angle Scattering Biological Data Bank (SASBDB; Kikhney *et al.*, 2020; Valentini *et al.*, 2015) with the accession codes SASDMS5(G-Rrm4) and SASDMT5 (H-Rrm4-NT4).

573 **Isothermal titration calorimetry**

574 All ITC experiments were performed as per the previous report (Abts *et al.*, 2013). All the
575 protein samples used in ITC were centrifuged at 451,000 g for 30 minutes and quantified by
576 Nanodrop (A280) before use. The concentration of GST-MLLE variants was adjusted to 30 µM
577 and PAM2 peptide variants was adjusted to 300 µM using buffer G (20 mM HEPES pH 8.0,
578 200 mM NaCl, 1 mM 2 ME) at 25°C.Using an MicroCal iTC200 titration calorimeter (Malvern
579 Panalytical technologies), a PAM2 peptide variant with a volume of 40 µL was titrated to the
580 different GST-MLLE variants. All experiments were repeated at least twice. ITC measurements
581 were performed at 25 °C with 40 injections (1 µL each). Only the first injection had a volume
582 of 0.5 µL and was discarded from the isotherm. The other technical parameters were reference
583 power, 5 µcal s^{-1}; stirring speed, 1000 rpm; spacing time, 120 s, and a filter period, 5 s. The
584 resulting isotherm was fitted with a one-site binding model using MicroCal Origin for ITC
585 software (MicroCal LLC).

586 **Microscopy, image processing and image analysis**

587 Laser-based epifluorescence-microscopy was performed on a Zeiss Axio Observer.Z1 as
588 previously described (Jankowski *et al.*, 2019). Co-localisation studies of dynamic processes
589 were carried out with a two-channel imager (DV2, Photometrics, Tucson, AZ, USA; Baumann
590 *et al.*, 2016). To quantify uni- and bipolar hyphal growth, cells were grown in 30 ml cultures to
591 an OD_{600} of 0.5, and hyphal growth was induced. After 6 hours, more than 100 hyphae were
592 analysed per strains towards their growth behaviour (n = 3). Cells were assessed for unipolar
593 and bipolar growth as well as the formation of a basal septum. To analyse the signal number,
594 velocity, and travelled distance of fluorescently labelled proteins, movies with an exposure time
595 of 150 ms and 150 frames were recorded. More than 25 hyphae were analysed per strain (n =
596 3). All movies and images were possessed and analysed using the Metamorph software (Version
597 7.7.0.0, Molecular Devices, Seattle, IL, USA). For the generation of kymographs, 20 µm of
598 hyphal cell starting at the hyphal tip were used. For statistical analysis of signal number,
599 velocity, and travelled distance, processive signals with a travelled distance of more than 5 µm
600 were conducted and counted manually. Data points represent means from three independent
601 experiments (n = 3) with mean of means (red line) and SEM. For all statistical evaluations, two-
602 tailed Student´s *t*-tests were used.
603

Acknowledgements

We thank Drs. Florian Altegoer and Dierk Niessing as well as laboratory members for critical reading of the manuscript. We acknowledge Drs. Georg Groth, Alexander Minges, and Mohan Gopalswamy for support with ITC experiments. We gratefully acknowledge the computational support provided by the "Center for Information and Media Technology" (ZIM) at the Heinrich Heine University Düsseldorf and the computing time provided by the John von Neumann Institute for Computing (NIC) on the supercomputer JUWELS at Jülich Supercomputing Centre (JSC) (user IDs: HKF7, VSK33). The synchrotron MX data were collected at ESRF ID23-EH1. We thank Sylvain Engilberge for the assistance in using the beamline. The final SAXS experiments were performed on beamline BM29 at the European Synchrotron Radiation Facility (ESRF), Grenoble, France. We are grateful to Dihia Moussaoui at the ESRF for providing assistance during data collection. The work was funded by grants from the Deutsche Forschungsgemeinschaft under Germany's Excellence Strategy EXC-2048/1 - Project ID 39068111 to MF; Project-ID 267205415 – SFB 1208 to MF (project A09), HG (project A03), and LS (project A01). The Center for Structural Studies is funded by the Deutsche Forschungsgemeinschaft (DFG Grant number 417919780; INST 208/740-1 FUGG; INST 208/761-1 FUGG).

Author contributions

SKD, SSV, LS, SHJS, HG, and MF designed this study and analysed the data. SKD and SSV contributed equally to the structural biology of the MLLE binding platform; SKD performed the wet lab experiments and SSV was responsible for modelling. KM and SKD performed the cell biological experiments. LB coordinated strain generation and experimental design. JR, EH, AH contributed to SAXS, MALS, and X ray analysis, respectively. SKD, SSV, LS, SHJS, HG, and MF drafted and revised the manuscript with input from all co-authors. SKD, SSV, SHJS, HG and MF directed the project.

Conflict of interest

The authors declare that they have no competing interests.

634 **References**

635 Abts A, Montalban-Lopez M, Kuipers OP, Smits SH, Schmitt L (2013) NisC binds the FxLx
636 motif of the nisin leader peptide. *Biochemistry* 52: 5387-5395
637 Afonine PV, Grosse-Kunstleve RW, Echols N, Headd JJ, Moriarty NW, Mustyakimov M,
638 Terwilliger TC, Urzhumtsev A, Zwart PH, Adams PD (2012) Towards automated
639 crystallographic structure refinement with phenix.refine. *Acta Crystallogr D Biol*
640 *Crystallogr* 68: 352-367
641 Albrecht M, Lengauer T (2004) Survey on the PABC recognition motif PAM2. *Biochem*
642 *Biophys Res Commun* 316: 129-138
643 Baek M, DiMaio F, Anishchenko I, Dauparas J, Ovchinnikov S, Lee GR, Wang J, Cong Q,
644 Kinch LN, Schaeffer RD *et al.* (2021) Accurate prediction of protein structures and
645 interactions using a three-track neural network. *Science* 373: 871-876
646 Baumann S, König J, Koepke J, Feldbrügge M (2014) Endosomal transport of septin mRNA
647 and protein indicates local translation on endosomes and is required for correct septin
648 filamentation. *EMBO Rep* 15: 94-102
649 Baumann S, Pohlmann T, Jungbluth M, Brachmann A, Feldbrügge M (2012) Kinesin-3 and
650 dynein mediate microtubule-dependent co-transport of mRNPs and endosomes. *J Cell Sci*
651 125: 2740-2752
652 Baumann S, Zander S, Weidtkamp-Peters S, Feldbrügge M (2016) Live cell imaging of septin
653 dynamics in *Ustilago maydis*. In: *Methods in Cell Biol: Septins*, Gladfelter A.S. (ed.) pp.
654 143-159. Elsevier Inc.:
655 Becht P, König J, Feldbrügge M (2006) The RNA-binding protein Rrm4 is essential for polarity
656 in *Ustilago maydis* and shuttles along microtubules. *J Cell Sci* 119: 4964-4973
657 Béthune J, Jansen RP, Feldbrügge M, Zarnack K (2019) Membrane-associated RNA-binding
658 proteins orchestrate organelle-coupled translation *Trends in cell biology* 29: 178-188
659 Brachmann A, König J, Julius C, Feldbrügge M (2004) A reverse genetic approach for
660 generating gene replacement mutants in *Ustilago maydis*. *Mol Gen Genom* 272: 216-226
661 Brachmann A, Weinzierl G, Kämper J, Kahmann R (2001) Identification of genes in the bW/bE
662 regulatory cascade in *Ustilago maydis*. *Mol Microbiol* 42: 1047-1063
663 Cioni JM, Lin JQ, Holtermann AV, Koppers M, Jakobs MAH, Azizi A, Turner-Bridger B,
664 Shigeoka T, Franze K, Harris WA *et al.* (2019) Late endosomes act as mRNA translation
665 platforms and sustain mitochondria in axons. *Cell* 176: 56-72 e15
666 Das S, Vera M, Gandin V, Singer RH, Tutucci E (2021) Intracellular mRNA transport and
667 localized translation. *Nat Rev Mol Cell Biol* 22: 483-504

668 Deo RC, Sonenberg N, Burley SK (2001) X-ray structure of the human hyperplastic discs
669 protein: an ortholog of the C-terminal domain of poly(A)-binding protein. *Proc Natl Acad*
670 *Sci U S A* 98: 4414-4419
671 Emsley P, Cowtan K (2004) Coot: model-building tools for molecular graphics. *Acta*
672 *Crystallogr D Biol Crystallogr* 60: 2126-2132
673 Fernandopulle MS, Lippincott-Schwartz J, Ward ME (2021) RNA transport and local
674 translation in neurodevelopmental and neurodegenerative disease. *Nature neuroscience*
675 Franke D, Petoukhov MV, Konarev PV, Panjkovich A, Tuukkanen A, Mertens HDT, Kikhney
676 AG, Hajizadeh NR, Franklin JM, Jeffries CM *et al.* (2017) ATSAS 2.8: a comprehensive
677 data analysis suite for small-angle scattering from macromolecular solutions. *J Appl*
678 *Crystallogr* 50: 1212-1225
679 Franke D, Svergun DI (2009) DAMMIF, a program for rapid ab-initio shape determination in
680 small-angle scattering. *J Appl Crystallogr* 42: 342-346
681 Grimm C, Pelz JP, Schneider C, Schaffler K, Fischer U (2020) Crystal structure of a variant
682 PAM2 motif of LARP4B bound to the MLLE domain of PABPC1. *Biomol* 10
683 Haag C, Steuten B, Feldbrügge M (2015) Membrane-coupled mRNA trafficking in fungi. *Annu*
684 *Rev Microbiol* 69: 265-281
685 Jankowski S, Pohlmann T, Baumann S, Müntjes KM, Devan SK, Zander S, Feldbrügge M
686 (2019) The multi PAM2 protein Upa2 functions as novel core component of endosomal
687 mRNA transport. *EMBO Rep* 24: e47381
688 Jinek M, Fabian MR, Coyle SM, Sonenberg N, Doudna JA (2010) Structural insights into the
689 human GW182-PABC interaction in microRNA-mediated deadenylation. *Nat Struct Mol*
690 *Biol* 17: 238-240
691 Jumper J, Evans R, Pritzel A, Green T, Figurnov M, Ronneberger O, Tunyasuvunakool K, Bates
692 R, Zidek A, Potapenko A *et al.* (2021) Highly accurate protein structure prediction with
693 AlphaFold. *Nature* 596: 583-589
694 Kabsch W (2014) Processing of X-ray snapshots from crystals in random orientations. *Acta*
695 *Crystallogr D Biol Crystallogr* 70: 2204-2216
696 Kikhney AG, Borges CR, Molodenskiy DS, Jeffries CM, Svergun DI (2020) SASBDB:
697 Towards an automatically curated and validated repository for biological scattering data.
698 *Protein Sci* 29: 66-75
699 Konarev PV, Volkov VV, Sokolova AV, Koch MHJ, Svergun DI (2003) PRIMUS: a Windows
700 PC-based system for small-angle scattering data analysis. *J Appl Crystallogr* 36: 1277-
701 1282

702 Kozlov G, De Crescenzo G, Lim NS, Siddiqui N, Fantus D, Kahvejian A, Trempe JF, Elias D,
703 Ekiel I, Sonenberg N *et al.* (2004) Structural basis of ligand recognition by PABC, a highly
704 specific peptide-binding domain found in poly(A)-binding protein and a HECT ubiquitin
705 ligase. *EMBO J* 23: 272-281
706 Kozlov G, Gehring K (2010) Molecular basis of eRF3 recognition by the MLLE domain of
707 poly(A)-binding protein. *PLoS One* 5: e10169
708 Kozlov G, Menade M, Rosenauer A, Nguyen L, Gehring K (2010) Molecular determinants of
709 PAM2 recognition by the MLLE domain of poly(A)-binding protein. *J Mol Biol* 397: 397-
710 407
711 Kozlov G, Trempe JF, Khaleghpour K, Kahvejian A, Ekiel I, Gehring K (2001) Structure and
712 function of the C-terminal PABC domain of human poly(A)-binding protein. *Proc Natl*
713 *Acad Sci U S A* 98: 4409-4413
714 Liao YC, Fernandopulle MS, Wang G, Choi H, Hao L, Drerup CM, Patel R, Qamar S, Nixon-
715 Abell J, Shen Y *et al.* (2019) RNA granules hitchhike on lysosomes for long-distance
716 transport, using annexin A11 as a molecular tether. *Cell* 179: 147-164 e120
717 Lim NS, Kozlov G, Chang TC, Groover O, Siddiqui N, Volpon L, De Crescenzo G, Shyu AB,
718 Gehring K (2006) Comparative peptide binding studies of the PABC domains from the
719 ubiquitin-protein isopeptide ligase HYD and poly(A)-binding protein. Implications for
720 HYD function. *The Journal of biological chemistry* 281: 14376-14382
721 Loubradou G, Brachmann A, Feldbrügge M, Kahmann R (2001) A homologue of the
722 transcriptional repressor Ssn6p antagonizes cAMP signalling in *Ustilago maydis. Mol*
723 *Microbiol* 40: 719-730
724 Manalastas-Cantos K, Konarev PV, Hajizadeh NR, Kikhney AG, Petoukhov MV, Molodenskiy
725 DS, Panjkovich A, Mertens HDT, Gruzinov A, Borges C *et al.* (2021) ATSAS 3.0:
726 expanded functionality and new tools for small-angle scattering data analysis. *J Appl*
727 *Crystallogr* 54
728 Mangus DA, Amrani N, Jacobson A (1998) Pbp1p, a factor interacting with *Saccharomyces*
729 *cerevisiae* poly(A)-binding protein, regulates polyadenylation. *Molecular and cellular*
730 *biology* 18: 7383-7396
731 Mangus DA, Evans MC, Jacobson A (2003) Poly(A)-binding proteins: multifunctional
732 scaffolds for the post-transcriptional control of gene expression. *Genome Biol* 4: 223
733 Mattijssen S, Kozlov G, Fonseca BD, Gehring K, Maraia RJ (2021) LARP1 and LARP4: up
734 close with PABP for mRNA 3' poly(A) protection and stabilization. *RNA Biol* 18: 259-274
735 Mofatteh M, Bullock SL (2017) SnapShot: Subcellular mRNA localization. *Cell* 169: 178.e171

736 Müller J, Pohlmann T, Feldbrügge M (2019) Core components of endosomal mRNA transport
737 are evolutionarily conserved in fungi. *Fungal Genet Biol* 126: 12-16
738 Mulnaes D, Gohlke H (2018) TopScore: using deep neural networks and large diverse data sets
739 for accurate protein model quality assessment. *J Chem Theory Comput* 14: 6117-6126
740 Mulnaes D, Koenig F, Gohlke H (2021) TopSuite Web Server: A Meta-Suite for Deep-
741 Learning-Based Protein Structure and Quality Prediction. *Journal of chemical information*
742 *and modeling* 61: 548-553
743 Mulnaes D, Porta N, Clemens R, Apanasenko I, Reiners J, Gremer L, Neudecker P, Smits SHJ,
744 Gohlke H (2020a) TopModel: template-based protein structure prediction at low sequence
745 identity using top-down consensus and deep neural networks. *J Chem Theory Comput* 16:
746 1953-1967
747 Mulnaes D, Porta N, Clemens R, Apanasenko I, Reiners J, Gremer L, Neudecker P, Smits SHJ,
748 Gohlke H (2020b) TopModel: Template-Based Protein Structure Prediction at Low
749 Sequence Identity Using Top-Down Consensus and Deep Neural Networks. *J Chem*
750 *Theory Comput* 16: 1953-1967
751 Munoz-Escobar J, Matta-Camacho E, Kozlov G, Gehring K (2015) The MLLE domain of the
752 ubiquitin ligase UBR5 binds to its catalytic domain to regulate substrate binding. *The*
753 *Journal of biological chemistry* 290: 22841-22850
754 Müntjes K, Devan SK, Reichert AS, Feldbrügge M (2021) Linking transport and translation of
755 mRNAs with endosomes and mitochondria. *EMBO reports* accepted for publication
756 Müntjes K, Philipp M, Husemann L, Heucken N, Weidtkamp-Peters S, Schipper K, Zurbriggen
757 MD, Feldbrügge M (2020) Establishing polycistronic expression in the model
758 microorganism *Ustilago maydis*. *Front Microbiol* 11: 1384
759 Niessing D, Jansen RP, Pohlmann T, Feldbrügge M (2018) mRNA transport in fungal top
760 models. *Wiley interdisciplinary reviews RNA* 9: e1453
761 Olgeiser L, Haag C, Boerner S, Ule J, Busch A, Koepke J, König J, Feldbrügge M, Zarnack K
762 (2019) The key protein of endosomal mRNP transport Rrm4 binds translational landmark
763 sites of cargo mRNAs. *EMBO Rep* 20: e46588
764 Pernot P, Round A, Barrett R, De Maria Antolinos A, Gobbo A, Gordon E, Huet J, Kieffer J,
765 Lentini M, Mattenet M *et al.* (2013) Upgraded ESRF BM29 beamline for SAXS on
766 macromolecules in solution. *Journal of synchrotron radiation* 20: 660-664
767 Pernot P, Theveneau P, Giraud T, Fernandes RN, Nurizzo D, Spruce D, Surr J, McSweeney S,
768 Round A, Felisaz F *et al.* (2010) New beamline dedicated to solution scattering from

769 biological macromolecules at the ESRF. *Journal of Physics: Conference Series* 247:
770 012009
771 Pohlmann T, Baumann S, Haag C, Albrecht M, Feldbrügge M (2015) A FYVE zinc finger
772 domain protein specifically links mRNA transport to endosome trafficking. *eLife* 4: e06041
773 Quentin D, Schuhmacher JS, Klink BU, Lauer J, Shaikh TR, Huis in t´t Veld PJ, Welp LM,
774 Urlaub H, Zerial M, Raunser S (2021) Structure of the human FERRY Rab5 effector
775 complex. *bioRiv* 10.1101/2021.06.21.449265
776 Sawazaki R, Imai S, Yokogawa M, Hosoda N, Hoshino SI, Mio M, Mio K, Shimada I, Osawa
777 M (2018) Characterization of the multimeric structure of poly(A)-binding protein on a
778 poly(A) tail. *Sci Rep* 8: 1455
779 Schäfer IB, Yamashita M, Schuller JM, Schussler S, Reichelt P, Strauss M, Conti E (2019)
780 Molecular bsis for poly(A) RNP architecture and recognition by the Pan2-Pan3
781 deadenylase. *Cell* 177: 1619-1631 e1621
782 Schuhmacher JS, Dieck ST, Christoforidis S, Landerer C, Hersemann L, Seifert S, Giner A,
783 Toth-Petroczy A, Kalaidzidis Y, Schumann EM *et al.* (2021) The novel Rab5 effector
784 FERRY links early endosomes with the translation machinery. *BioRiv*
785 10.1101/2021.06.20.449167
786 Slotboom DJ, Duurkens RH, Olieman K, Erkens GB (2008) Static light scattering to
787 characterize membrane proteins in detergent solution. *Methods* 46: 73-82
788 Stenmark H, Aasland R, Driscoll PC (2002) The phosphatidylinositol 3-phosphate-binding
789 FYVE finger. *FEBS Lett* 513: 77-84
790 Studier FW (2005) Protein production by auto-induction in high density shaking cultures.
791 *Protein Expr Purif* 41: 207-234
792 Su H, Meng S, Lu Y, Trombly MI, Chen J, Lin C, Turk A, Wang X (2011) Mammalian
793 hyperplastic discs homolog EDD regulates miRNA-mediated gene silencing. *Mol Cell* 43:
794 97-109
795 Svergun DI (1992) Determination of the regularization parameter in indirect-transform methods
796 using perceptual criteria. . *J Appl Crystallogr* 25: 495-503
797 Terfrüchte M, Joehnk B, Fajardo-Somera R, Braus G, Riquelme M, Schipper K, Feldbrügge M
798 (2014) Establishing a versatile Golden Gate cloning system for genetic engineering in
799 fungi. *Fungal Genet Biol* 62: 1-10
800 Tian L, Chou HL, Fukuda M, Kumamaru T, Okita TW (2020a) mRNA localization in plant
801 cells. *Plant Physiol* 182: 97-109

802 Tian L, Chou HL, Zhang L, Hwang SK, Starkenburg SR, Doroshenk KA, Kumamaru T, Okita
803 TW (2018) RNA-binding protein RBP-P is required for glutelin and prolamine mRNA
804 localization in rice endosperm cells. *Plant Cell* 30: 2529-2552
805 Tian L, Doroshenk KA, Zhang L, Fukuda M, Washida H, Kumamaru T, Okita T (2020b)
806 Zipcode RNA-binding proteins and membrane trafficking proteins cooperate to transport
807 glutelin mRNAs in rice endosperm. *Plant Cell* 32: 2566-2581
808 Tria G, Mertens HD, Kachala M, Svergun DI (2015) Advanced ensemble modelling of flexible
809 macromolecules using X-ray solution scattering. *IUCrJ* 2: 207-217
810 Valentini E, Kikhney AG, Previtali G, Jeffries CM, Svergun DI (2015) SASBDB, a repository
811 for biological small-angle scattering data. *Nucleic Acids Res* 43: D357-363
812 Weiler AJ, Spitz O, Gudzuhn M, Schott-Verdugo SN, Kamel M, Thiele B, Streit RW, Kedrov
813 A, L. S, Gohlke H *et al.* (2021) Novel intracellular phospholipase B from *Pseudomonas*
814 *aeruginosa* with activity towards endogenous phospholipids affects biofilm assembly.
815 *bioRiv* doi.org/10.1101/2021.06.15.448513
816 Xie J, Kozlov G, Gehring K (2014) The "tale" of poly(A) binding protein: the MLLE domain
817 and PAM2-containing proteins. *Biochim Biophys Acta* 1839: 1062-1068
818 Yang R, Gaidamakov SA, Xie J, Lee J, Martino L, Kozlov G, Crawford AK, Russo AN, Conte
819 MR, Gehring K *et al.* (2011) La-related protein 4 binds poly(A), interacts with the poly(A)-
820 binding protein MLLE domain via a variant PAM2w motif, and can promote mRNA
821 stability. *Mol Cell Biol* 31: 542-556
822 Zander S, Baumann S, Weidtkamp-Peters S, Feldbrügge M (2016) Endosomal assembly and
823 transport of heteromeric septin complexes promote septin cytoskeleton formation. *J Cell*
824 *Sci* 129: 2778-2792

825 **Figures**

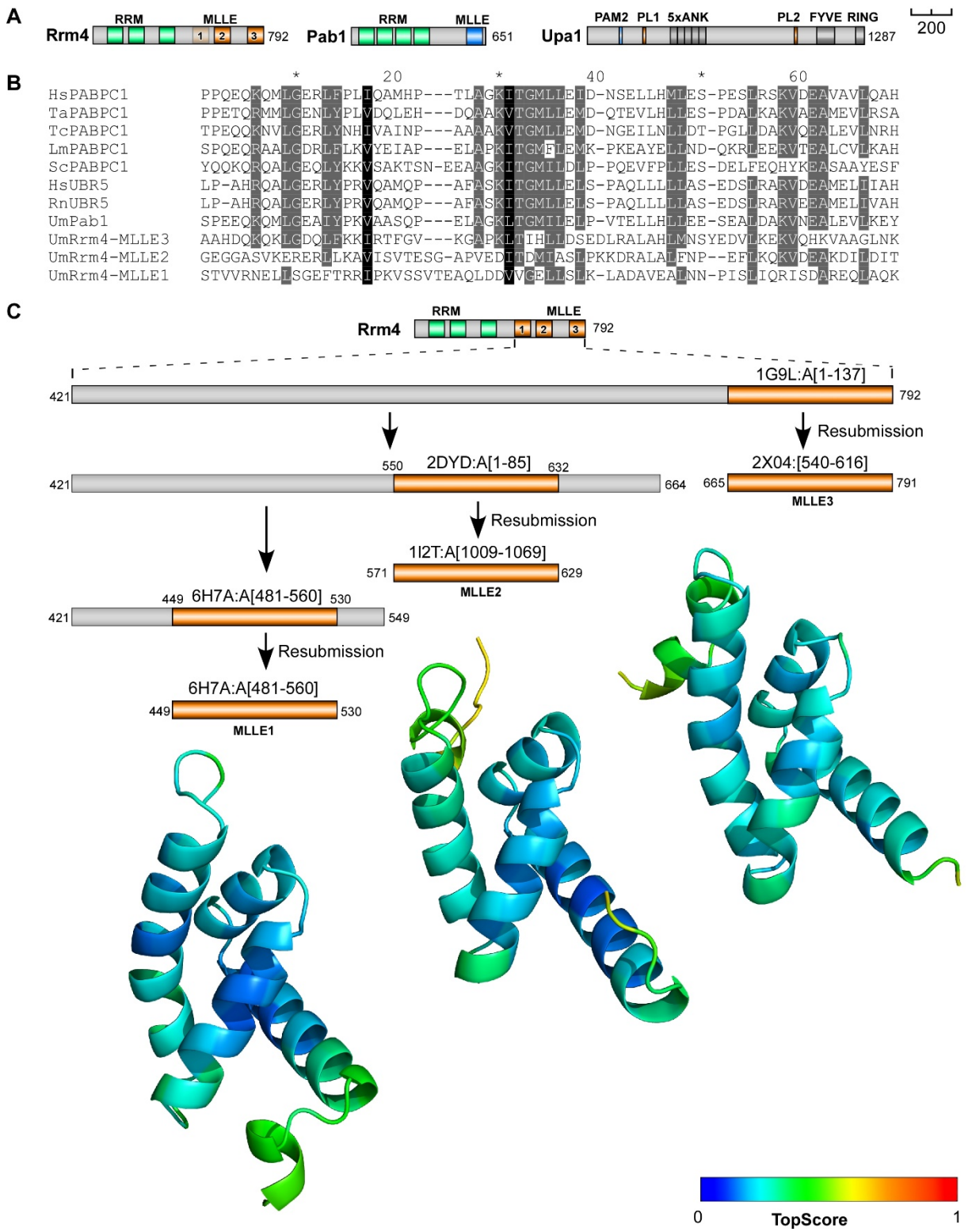

826

827 **Figure 1. The C-terminal half of Rrm4 contains three MLLE domains.**

828 (**A**) Schematic representation of protein variants drawn to scale (bar, 200 amino acids, number
829 of amino acids indicated next to protein bars) using the following colouring: dark green, RNA
830 recognition motif (RRM); orange, MLLE^{Rrm4} domains; dark blue, MLLE^{Pab1}; light blue PAM2;

light orange PAM2L sequence (PL1 – 2) Ankyrin repeats (5xANK), FYVE domain, and RING domain of Upa1 are given in dark grey. (**B**) Sequence alignment of previously determined MLLE domains showing the degree of similarity to the three Rrm4-MLLE domains and the positions (Hs - *Homo sapiens*, Ta - *Triticum aestivum*, La - *Leishmania major*, Sc - *Saccharomyces cerevisiae*, Tc - *Trypanosoma cruzi*, Rn - *Rattus norvegicus*, Um - *Ustilago maydis*, PABPC1, Pab1 – poly [A]-binding protein, UBR5 - E3 ubiquitin-protein ligase). Accession number and sequence coverage are listed in the Appendix Table S1. Multiple sequence alignment was performed by ClustalW. (**C)** Identification and modeling of C-terminal MLLE domains of Rrm4. The iterative process is depicted graphically. The best identified template for each run, and the region of that template that aligns with Rrm4, are displayed (see also Fig. EV1A for the templates used for the final models). The structural models obtained are shown for the span of the first identified template and are coloured according to their per-residue TopScore, where the scale from 0 to 1 indicates a low to high local structural error.

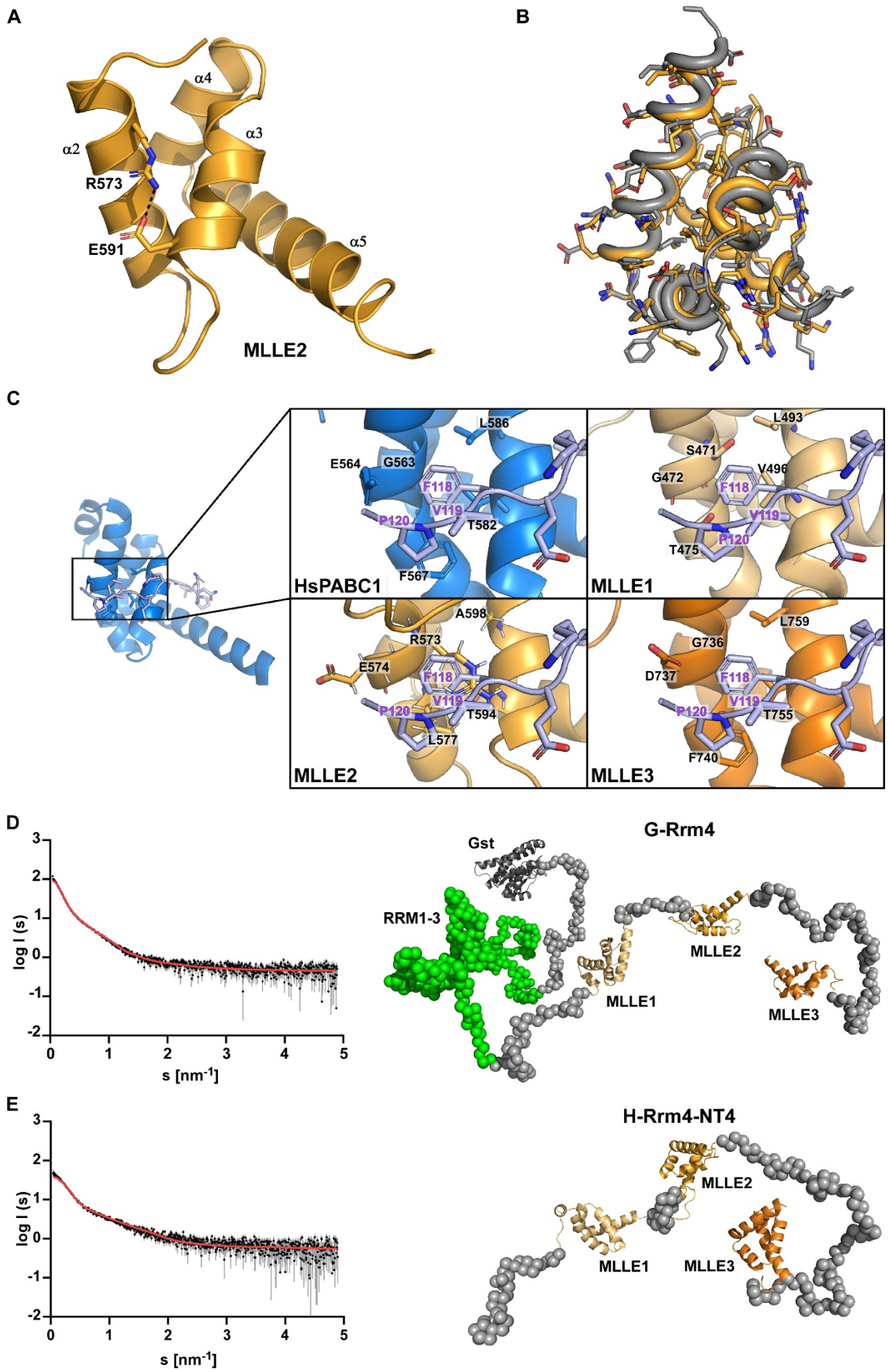
A
α4
α3
α2
R573
E591
α5
MLLE2
B
C
L586
E564
G563
F118
V119
P120
T582
F567
HsPABC1
L493
S471
G472
V496
F118
V119
P120
T475
MLLE1
A598
R573
E574
F118
V119
P120
T594
L577
MLLE2
L759
G736
D737
F118
V119
P120
T755
F740
MLLE3
D
log I (s)
s [nm-1]
G-Rrm4
Gst
RRM1-3
MLLE2
MLLE1
MLLE3
E
log I (s)
s [nm-1]
H-Rrm4-NT4
MLLE2
MLLE1
MLLE3

845

Figure 2. Rrm4 contains a C-terminal tripartite MLLE binding platform

(**A**) Crystal structure of the MLLE2 domain is highlighted in orange. The four helices are indicated by α2-5 according to the 5 helix nomenclature found in MLLE domains (Xie *et al.*, 2014). Note that the first short helix α1 is missing. Arg573 and Glu591 are highlighted in sticks. These sides chains would interfere with binding of the canonical Phe of PAM2 type motifs. (**B**) Structural alignment of the MLLE2 model generated by TopModel and the X-ray crystal structure of this domain (grey or orange, respectively). The all-atom RMSD is 0.69 Å, resulting mostly from different rotamers of solvent-exposed sidechains. (**C**) Comparison of peptide binding sites after structural alignment of the models of Rrm4 MLLE domains (orange shades) and the canonical MLLE domain of HsPABPC1 (blue; PDB ID 3KUS) and manually placing the PAM2 motif of PAIP2 (lilac). In the interaction of $MLLE^{PABPC1}$ with PAM2 of PAIP2, Phe118 of PAM2 is the major determinant for binding and present in all the PAM2 motifs except LARP4a and b (Kozlov & Gehring, 2010; Xie *et al.*, 2014; Fig. EV3A). Of the identified Rrm4 MLLE domains, only MLLE3 retains all sidechains that favour the binding of this characteristic Phe; particularly, Gly736 should allow the Phe to bind into a pocket. MLLE1 and MLLE2 have Ser471 and Arg573 instead of G in this position, suggesting that Phe binding would be sterically hindered in these interfaces. (**D**) *left panel* Experimental data curve for GST-Rrm4 is shown in black dots with grey error bars, the EOM fit as a red line (χ^2 =1.289). The intensity is displayed as a function of momentum transfers. *right panel*. Selected model of the EOM analysis from GST-Rrm4 with a R_g of 8.75 nm, a D_{max} of 23.99 nm with a volume fraction of~0.25. (**E**) *left panel* Experimental data curve for H-Rrm4NT4 is shown in black dots with grey error bars, the EOM fit as red line (χ^2 =1.262). The intensity is displayed as a function of momentum transfers. *right panel* Selected model of the EOM analysis from H-Rrm4NT4 with a R_g of 5.10 nm, a D_{max} of 16.43 nm, and a volume fraction of~0.75. The MLLE subdomains are shown in cartoon representation (MLLE1 in light orange, MLLE2 in orange, MLLE 3 in dark orange, and the GST in dark grey) and the missing amino acids as grey spheres (all other models and the SAXS data are available in Figure EV2E).

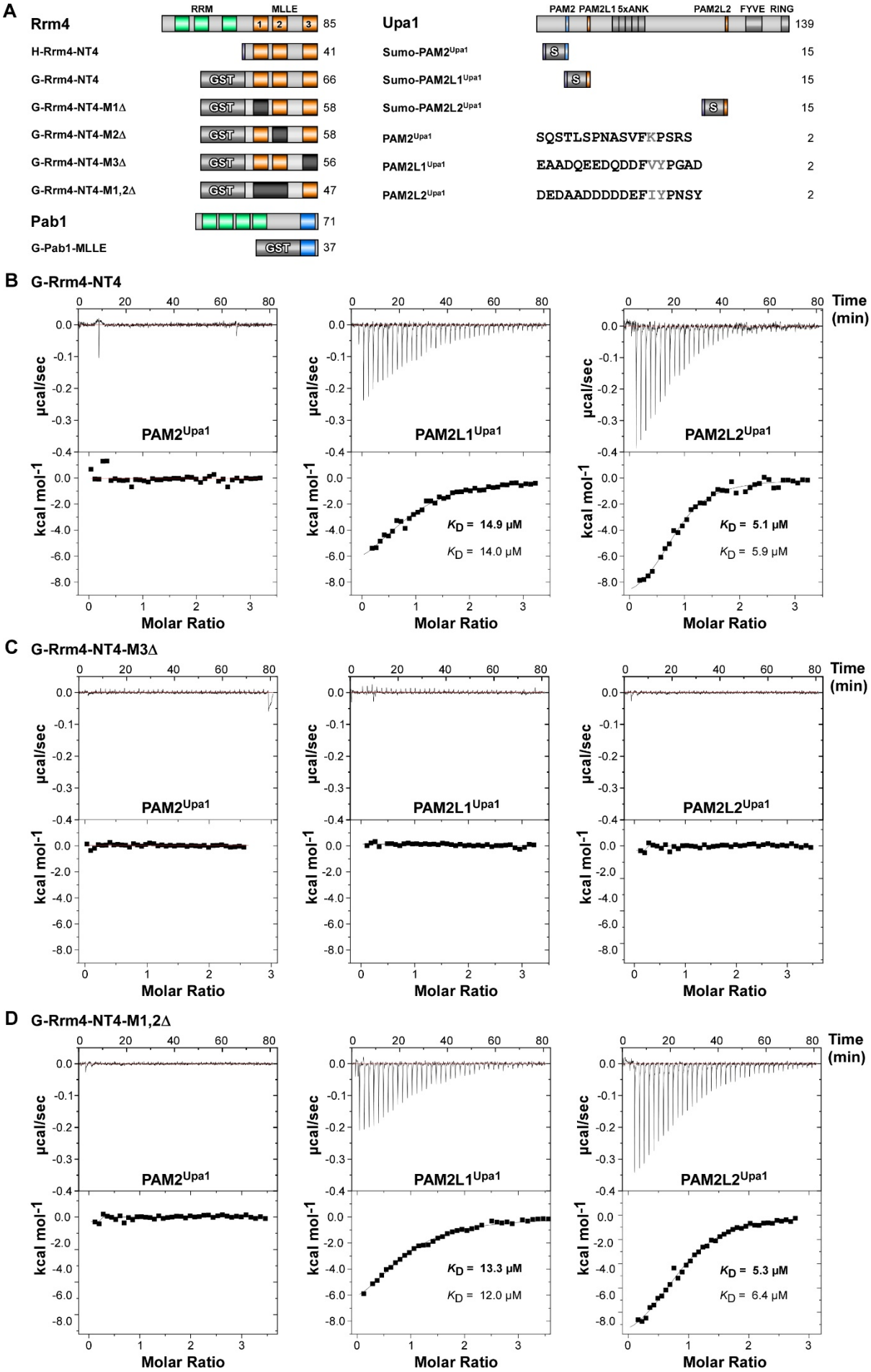
A
Rrm4
RRM
MLLE
1
2
3
85
H-Rrm4-NT4
41
G-Rrm4-NT4
GST
66
G-Rrm4-NT4-M1Δ
58
G-Rrm4-NT4-M2Δ
58
G-Rrm4-NT4-M3Δ
56
G-Rrm4-NT4-M1,2Δ
47
Pab1
71
G-Pab1-MLLE
37
Upa1
PAM2 PAM2L1 5xANK PAM2L2 FYVE RING
139
Sumo-PAM2Upa1
S
15
Sumo-PAM2L1Upa1
Sumo-PAM2L2Upa1
PAM2Upa1
SQSTLSPNASVFKPSRS
2
PAM2L1Upa1
EAADQEEDQDDFVYPGAD
PAM2L2Upa1
DEDAADDDDDEFIYPNSY
B G-Rrm4-NT4
C G-Rrm4-NT4-M3Δ
D G-Rrm4-NT4-M1,2Δ
Time (min)
µcal/sec
kcal mol-1
PAM2Upa1
PAM2L1Upa1
PAM2L2Upa1
KD = 14.9 µM
KD = 14.0 µM
KD = 5.1 µM
KD = 5.9 µM
KD = 13.3 µM
KD = 12.0 µM
KD = 5.3 µM
KD = 6.4 µM
Molar Ratio

875

876 **Figure 3. MLLE3^{Rrm4} is crucial for PAM2L1^{Upa1} and PAM2L2^{Upa1} binding.**

877 (**A**) Schematic representation of protein variants (Molecular weight in kilo Dalton indicated)
878 using the following colouring: dark green, RNA recognition motif (RRM); orange, MLLE^{Rrm4}
879 domains; dark blue, MLLE^{Pab1}; light blue PAM2; light orange PAM2L sequence (PL1 – 2).
880 Ankyrin repeats (5xANK), FYVE domain, and RING domain of Upa1 are given in dark grey.
881 GST and SUMO tags are labelled. Amino acids of the FxP and FxxP of PAM2 and PAM2L
882 sequences are printed in grey fond. (**B-D**) Representative isothermal titration calorimetry (ITC)
883 binding curves of MLLE domains. Experiments were performed using GST- or Histidine-
884 tagged MLLE variants and synthetic PAM2 peptide variants. K_D values of two independent
885 measurements are given (values corresponding to the indicated data are given in bold).
886

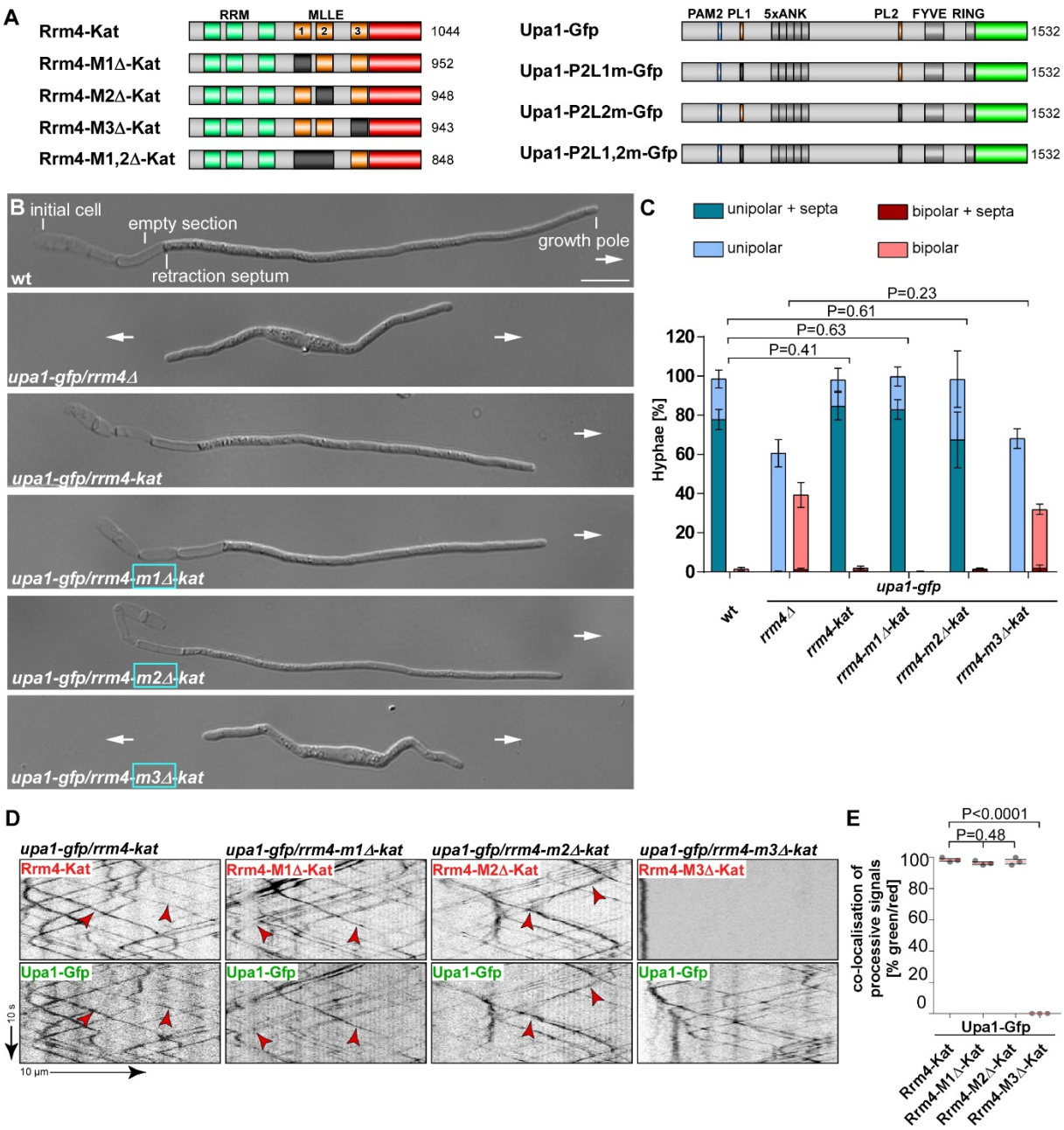

Figure 4. MLLE3 is key for endosomal mRNA transport.

(**A**) Schematic representation of Rrm4 and Upa1 variants drawn not to scale (number of amino acids indicated next to protein bars) using the following colouring: dark green, RNA recognition motif (RRM); orange, MLLE domains; red, mKate2, blue, PAM2, light orange PAM2 like sequence (PL1 – 2) and light green, Gfp. Ankyrin repeats (5xANK), FYVE domain and RING domain of Upa1 are given in dark grey. (**B**) Growth of AB33 derivatives in their hyphal form (6 h.p.i.; size bar 10 µm). Growth direction is marked by arrows. (**C**) Quantification of hyphal growth of AB33 derivatives shown in B (6 h.p.i.): unipolarity, bipolarity and basal septum formation were quantified (error bars, SEM.; n = 3 independent experiments, > 100 hyphae were counted per strain; for statistical evaluation, the percentage of uni- and bipolarity was investigated by using unpaired two-tailed Student's t-test ($\alpha<0.05$). (**D**) Kymographs of AB33 hyphae derivatives (6 h.p.i.; inverted fluorescence images) expressing pairs of red and green fluorescent proteins as indicated. Fluorescence signals were detected simultaneously using

901 dual-view technology (arrow length on the left and bottom indicates time and distance,
902 respectively). Processive co-localising signals are marked by red arrowheads. (**E**) Percentage
903 of processive signals exhibiting co-localisation for strains shown in D (data points represent
904 means from n = 3 independent experiments, with mean of means, red line and SEM; unpaired
905 two-tailed Student's t-test ($\alpha<0.05$); for each experiment, 10 hyphae per strains were analysed).
906
907

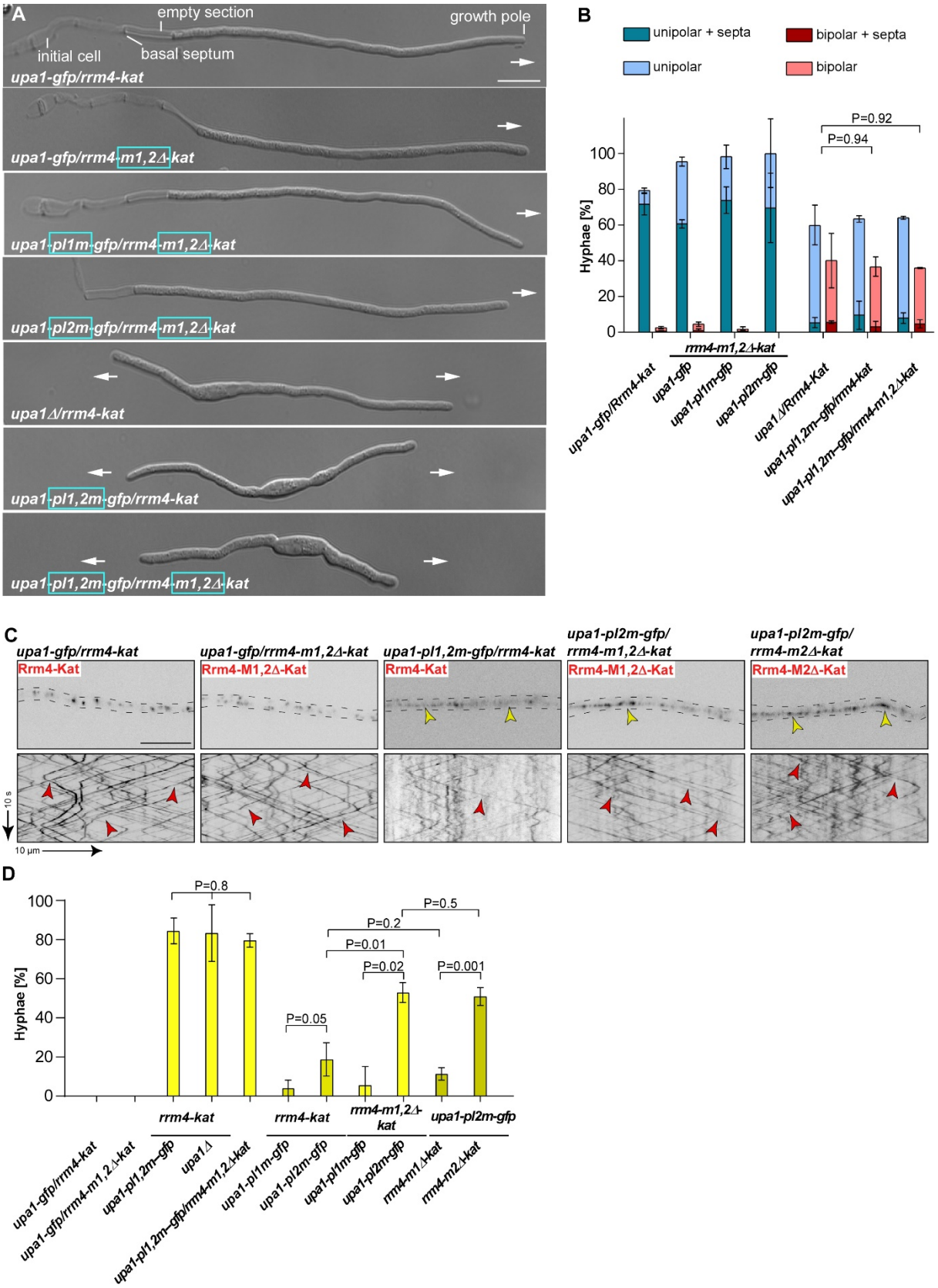

Figure 5. MLLE2 plays an accessory role in endosomal attachment of Rrm4

(**A**) Growth of AB33 derivatives in their hyphal form (6 h.p.i.; size bar 10 µm). Growth direction is marked by arrows. (**B**). Quantification of hyphal growth of AB33 derivatives shown in A (6 h.p.i.): unipolarity, bipolarity and basal septum formation were quantified (error bars,

913 SEM; n = 3 independent experiments, > 100 hyphae were analysed per strain; For statistical
914 analysis, the percentage of uni- and bipolarity was investigated by using unpaired two-tailed
915 Student's t-test ($\alpha<0.05$). (**C**) Micrographs (inverted fluorescence image; size bar, 10 µm) and
916 corresponding kymographs of AB33 hyphae derivatives (6 h.p.i.) co-expressing various Upa1-
917 Gfp and Rrm4-Kat versions as indicated. Movement of Rrm4-Kat versions is shown (arrow
918 length on the left and bottom indicates time and distance, respectively). Bidirectional movement
919 is visible as diagonal lines (red arrowheads). Aberrant microtubule staining is indicated by a
920 yellow arrowhead. (**D**) Percentage of hyphae (6 h.p.i.) exhibiting aberrant microtubule
921 association as indicated in panel C and EV5C. Set of strains that were analysed simultaneously
922 are shown in the same yellow shading (error bars, SEM; for statistical evaluation, the percentage
923 of hyphae with abnormal microtubule staining was compared by using unpaired two-tailed
924 Student's t-test ($\alpha<0.05$); n = 3 independent experiments, > 25 hyphae were analysed per
925 strain).
926
927

928 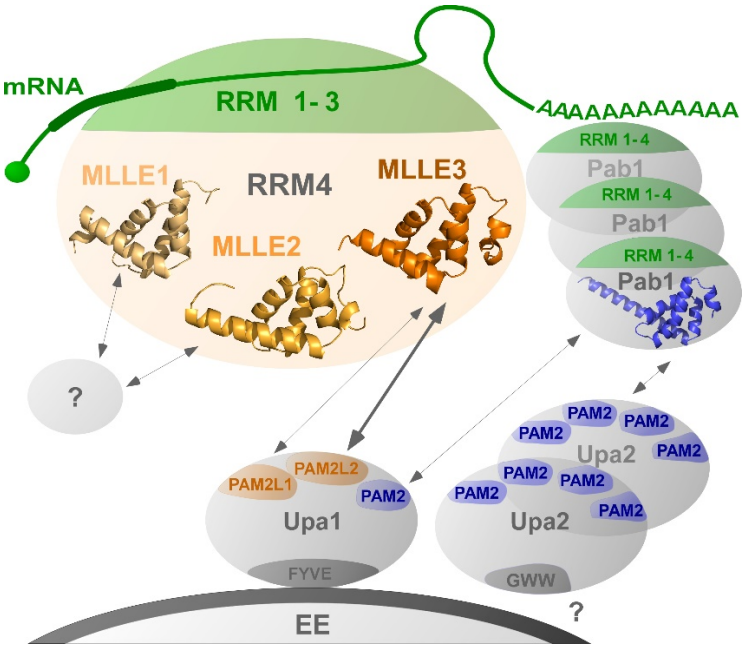

929 **Figure 6. Schematic model of endosomal attachment of mRNPs via MLLE domains**

930 Cargo mRNAs (green) are bound by the N-terminal RRM domains of Rrm4 (green). The C
931 terminal MLLE domains (orange) form a binding platform: MLLE3^{Rrm4} interacts with
932 PAM2L1^{Upa1} and PAM2L2^{Upa1}(orange), MLLE1 and -2^{Rrm4} might interact with a currently
933 unknown factor to support endosomal binding. The four RRMs of Pab1 (green) interact with
934 the poly(A) tail, and the MLLE^{Pab1} (blue) interacts with PAM2 of Upa1 and with the four PAM2
935 motifs of Upa2 (dark blue), a dimerising scaffold protein. Upa1 is attached to endosomes via
936 its FYVE domain, and the C-terminal GWW motif of Upa2 is crucial for its endosomal binding.
937

938 **Expanded View Figures**

A

Domain	Templates[a]	Rrm4 span	Template span	Identity (Similarity)[b]
MLLE1	6H7A:A	451-529	481-560	22.1 (38.4)
	3PTH:A	451-528	544-618	18.4 (34.5)
	1I2T:A	464-528	1009-1069	25.8 (40.9)
MLLE2	1I2T:A	571-629	1009-1069	23.8 (44.4)
	3KTP:A	550-631	554-620	17.6 (35.3)
	3KUR:A	550-627	554-616	18.5 (37.0)
MLLE3	2X04:A	712-791	540-616	30.6 (44.7)
	3KUR:A	716-791	544-616	32.9 (45.6)
	3KTP:A	716-791	544-616	32.9 (45.6)

a. PDB ID and chain identifier. b. in percentage

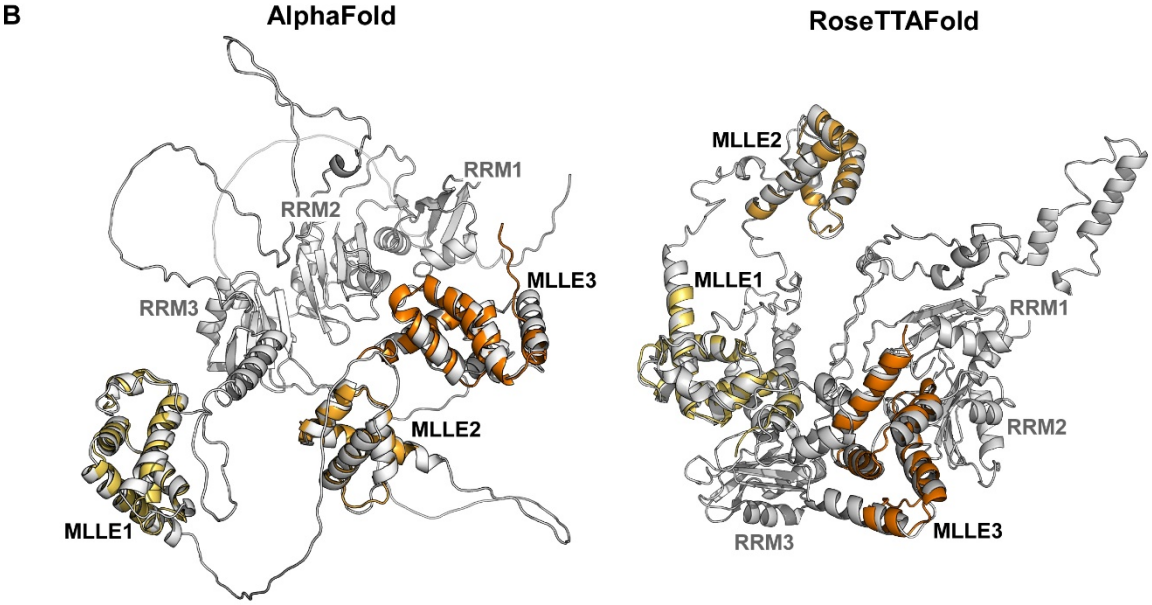

939

940 **Figure EV1. The presence of three MLLEs is verified by additional modeling predictions.**

941 (**A**) Compilation of MLLE sequences used for modeling with the highest similarity of MLLE1-
942 3^{Rrm4}. (**B**) Structural models obtained with TopModel overlaid to Rrm4 full-length models
943 obtained with the recently available tools as indicated. Natural alignments between
944 corresponding MLLE domains have an RMSD < 2Å, mutually confirming the quality of the
945 independently modeled structures. The differences in the relative domain arrangements in both
946 full-length models and the disordered regions in between the domains suggest a high mobility
947 within Rrm4.
948
949

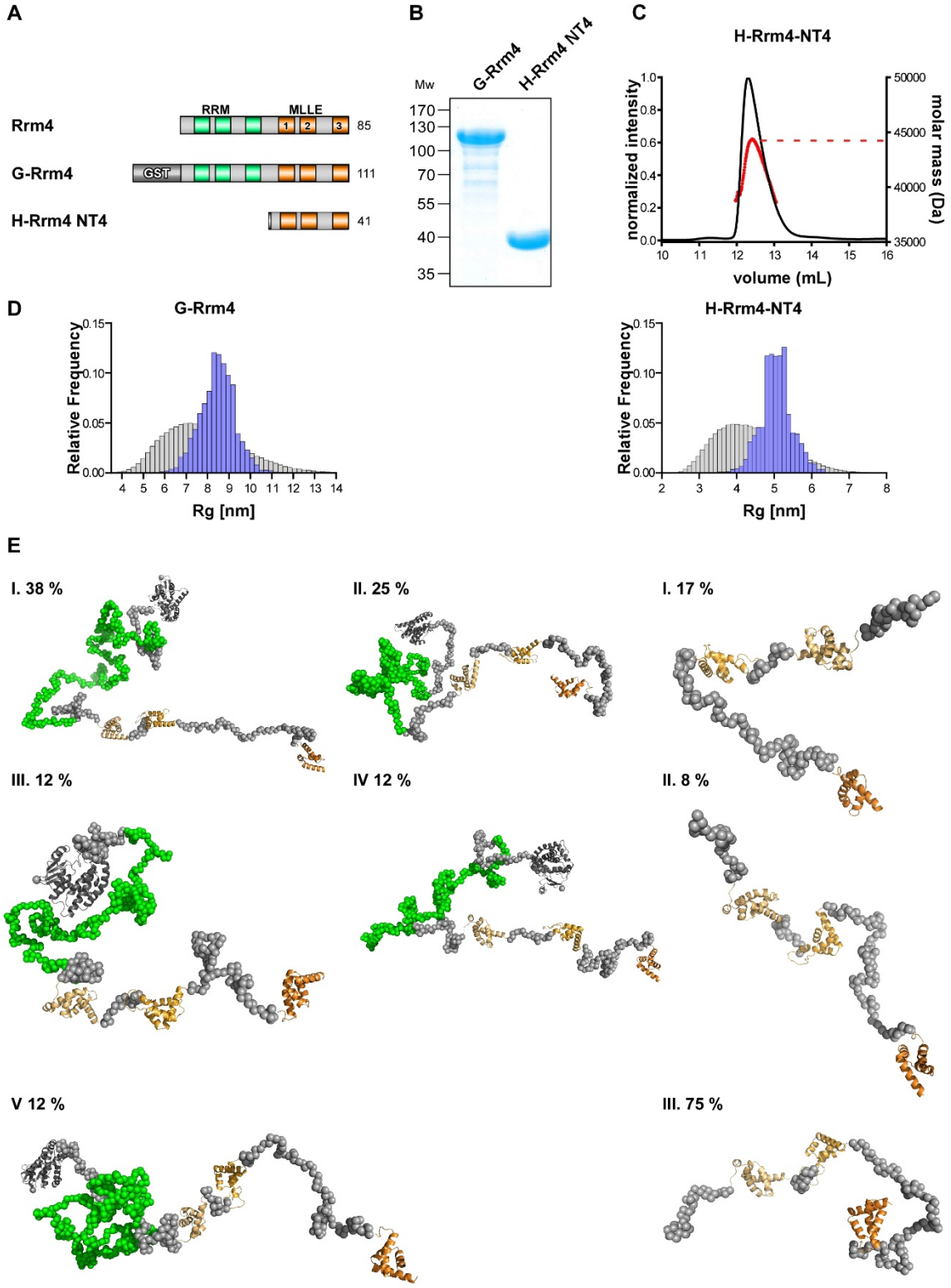

Figure EV2. The three MLLEs of Rrm4 are located in a flexible C-terminal region.

(**A**) Schematic representation of protein variants drawn to scale (molecular weight in kilo Dalton indicated next to protein bar) using the following coloring: dark green, RNA recognition motif (RRM); orange, MLLE^{Rrm4} domains; (**B**) SDS PAGE analysis of purified G-Rrm4, H-Rrm4-NT4 used in crystallography and SAXS measurement. (**C**) MALS-SEC analysis of H-Rrm4-NT4. Graph shows the elution profile. Dotted line in red indicate the apparent molecular

weight as observed in the light scattering. (**D**) R_g distribution calculated by EOM pool is shown in grey bars and the selected models in blue bars *left* GST_Rrm4 *right* H-Rrm4NT4 (**E**) *Left* Selected models of the EOM analysis for GST-Rrm4. The MLLE subdomains and the GST are shown in cartoon representation (MLLE1 in light orange, MLLE2 in orange, MLLE 3 in dark orange) and the missing amino acids as grey spheres. **I:** The model has a R_g of 8.94 nm, a D_{max} of 29.22 nm with a volume fraction of~0.38. **II:** The model has a R_g of 8.75 nm, a D_{max} of 23.99 with a volume fraction of~0.25. **III:** The model has a R_g of 7.74 nm, a D_{max} of 25.90 with a volume fraction of~0.12. **IV:** The model has a R_g of 8.33 nm, a D_{max} of 28.79 with a volume fraction of~0.12. **V:** The model has a R_g of 9.14 nm, a D_{max} of 33.73 with a volume fraction of~0.12. *Right* Selected models of the EOM analysis for H-Rrm4NT4. The MLLE subdomains are shown in cartoon representation (MLLE1 in light orange, MLLE2 in orange, MLLE3 in dark orange) and the missing amino acids as grey spheres. **I:** The model has a R_g of 5.12 nm, a D_{max} of 15.56 with a volume fraction of~0.17. **II:** The model has a R_g of 5.90 nm, a D_{max} of 18.73 nm with a volume fraction of~0.08. **III:** The model has a R_g of 5.10 nm, a D_{max} of 16.43 nm with a volume fraction of~0.75.

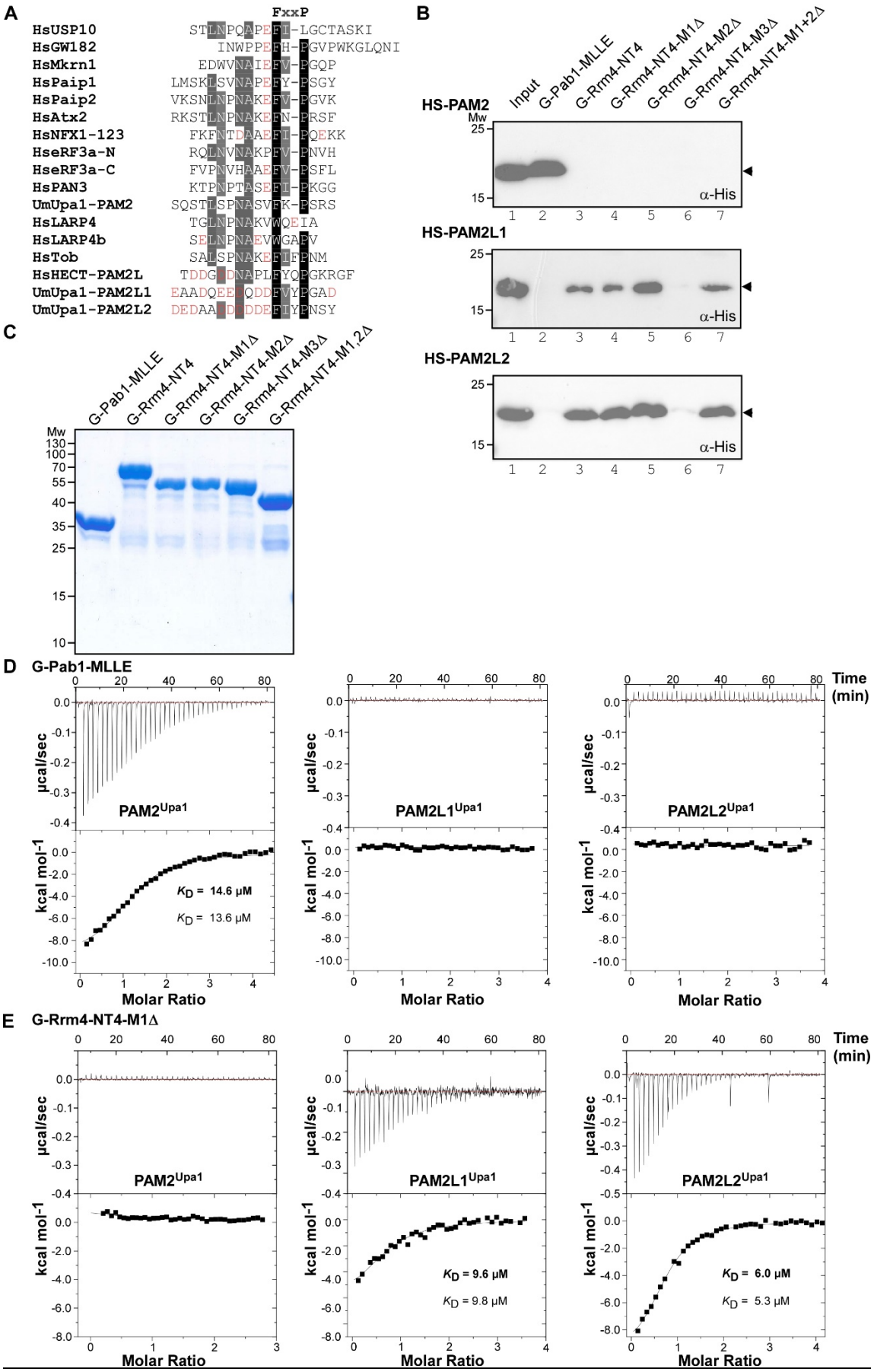

Continued on next page

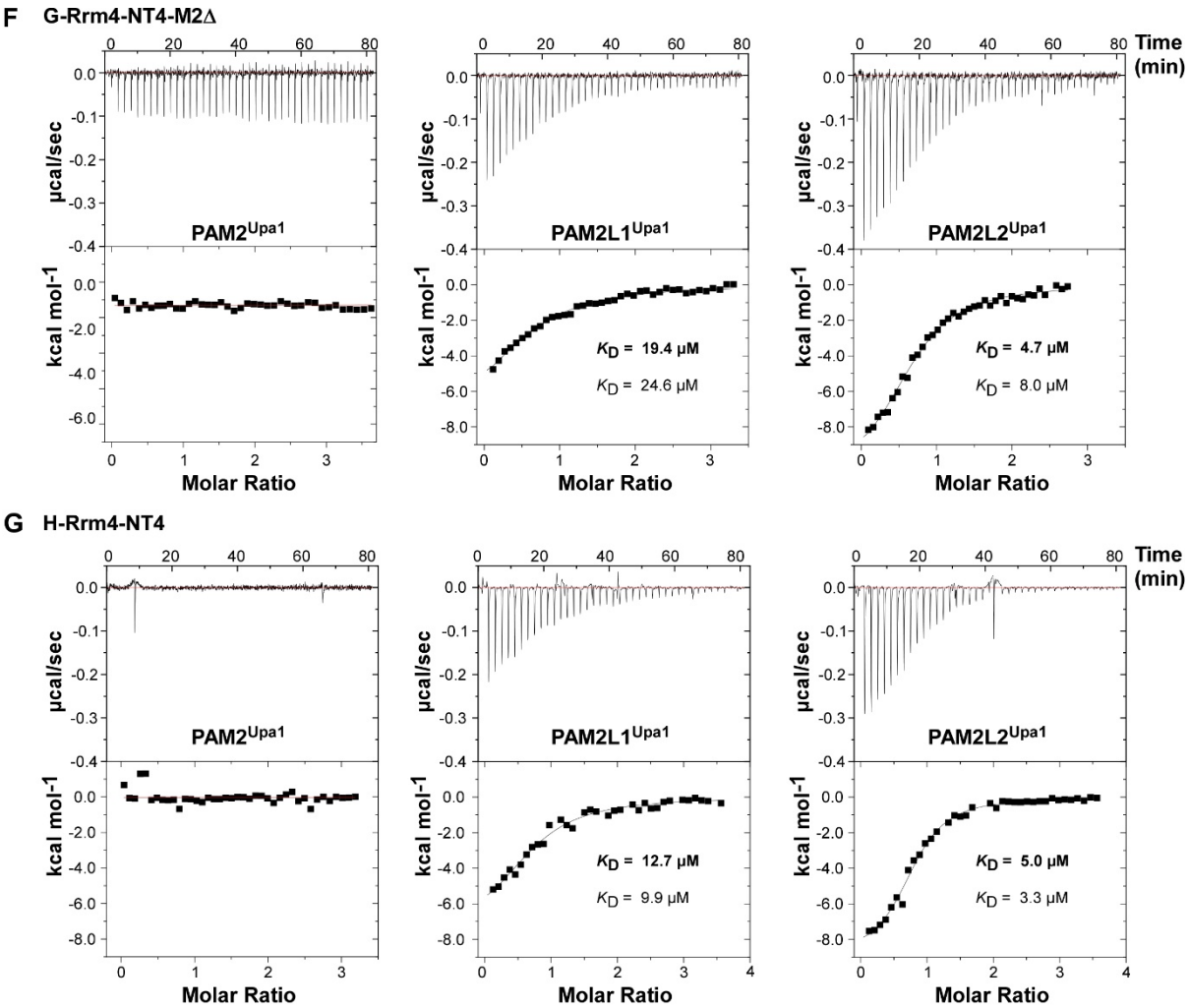

H

	PAM2^{Upa1}	PAM2L1^{Upa1}	PAM2L2^{Upa1}
G-Pab1-MLLE	14.6 / 13.6	No binding	No binding
G-Rrm4-NT4	No binding	14.9 / 14.0	5.1 / 5.9
G-Rrm4-NT4-M1Δ	No binding	9.6 / 9.8	6.0 / 5.3
G-Rrm4-NT4-M2Δ	No binding	19.4 / 24.6	4.7 / 8.0
G-Rrm4-NT4-M3Δ	No binding	No binding	No binding
G-Rrm4-NT4-M1,2Δ	No binding	13.3 / 12.0	5.3 / 6.4
H-Rrm4-NT4	No binding	12.7 / 9.9	5.0 / 3.3

Figure EV3. MLLE1^{Rrm4}, -2^{Rrm4} are not essential for PAM2L1^{Upa1} and -L2^{Upa1} binding.

(**A**) Comparison of PAM2 sequences found in Upa1 (UniprotKB ID A0A0D1E015) with those of human proteins, such as Usp10 (Q14694), GW182 Q9HCJ0), Mkrn1 (Q9UHC7), Paip1 (Q9H074), Paip2 (Q9BPZ3), Atx2 (-Q99700), NFX (Q12986), eRF3 (P15170), PAN3 (Q58A45), LARP4 (Q71RC2), LARP4b (Q92615), Tob (P50616), HECT (O95071), Asp and Glu are indicated in red stressing the highly negative charges in PAM2L sequences. (**B**)

982 Western blot analysis of GST co-purification experiments with components expressed in *E.*
983 *coli*: N-terminal Hexa-Histidine-SUMO-tagged PAM2 variants were pulled down by N-
984 terminal GST fused MLLE variants of Rrm4 and Pab1. Experiment was performed with the
985 soluble fraction of *E. coli* cell lysate to demonstrate specific binding. Results were analysed
986 with αHis immunoblotting (**C**) SDS PAGE analysis of purified GST-MLLE variants used in
987 ITC experiments (**D-G**) Representative isothermal titration calorimetry (ITC) binding curves
988 of MLLE domains. Experiments were performed using GST or hexa-histidine-tagged MLLE
989 variants and synthetic PAM2 peptide variants. K_D values of two independent measurements are
990 given (values corresponding to the indicated data are given in bold). (**H**) Summary of ITC
991 results shown in the Fig3 and Fig EV3. K_D values are given in μM.
992

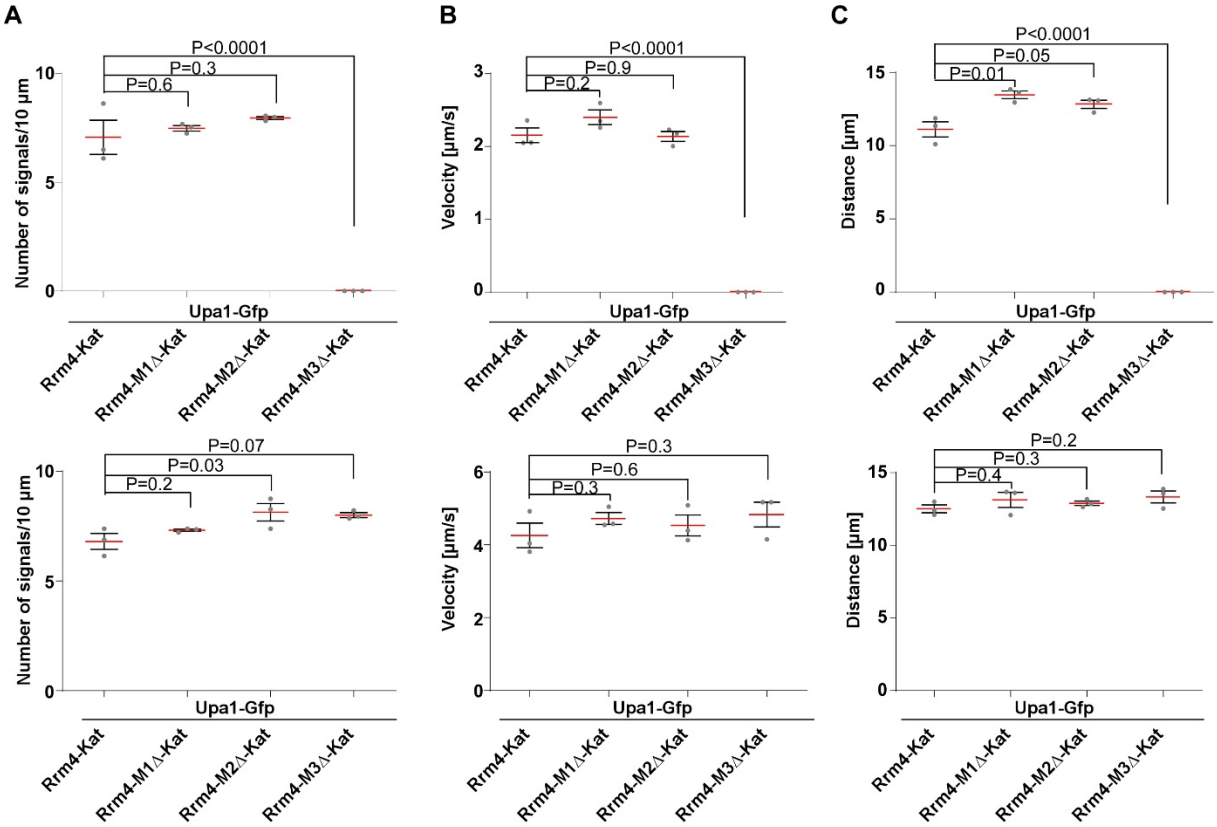

D

upa1	*rrm4*	Phenotype	Endosomal shuttling of Rrm4	Microtuble binding of Rrm4
wt	*wt*	*wt*	*wt*	*wt*
wt	*rrm4Δ*	bipolar	not applicable	not applicable
wt	*m1Δ*	*wt*	*wt*	*wt*
wt	*m2Δ*	*wt*	*wt*	*wt*
wt	*m3Δ*	bipolar	abolished	not applicable
wt	*wt*	*wt*	*wt*	*wt*
wt	*m1,2Δ*	*wt*	*wt*	*wt*
pl1,2m	*wt*	bipolar	aberrant	strong
upa1Δ	*wt*	bipolar	aberrant	strong
pl1,2m	*m1,2Δ*	bipolar	aberrant	strong
pl1m	*wt*	*wt*	*wt*	weak
pl2m	*wt*	*wt*	*wt*	medium
pl1m	*m1,2Δ*	*wt*	*wt*	weak
pl2m	*m1,2Δ*	*wt*	*wt*	strong
pl2m	*m1Δ*	bipolar	*wt*	medium
pl2m	*m2Δ*	bipolar	*wt*	strong

Figure EV4. Deletion of MLLE3^{Rrm4} abolishes endosomal movement of Rrm4

995 (**A-C**) Quantification of processive Rrm4-Kat (top) and Upa1-Gfp signals (bottom; (**A**)),
996 velocity of fluorescent Rrm4-Kat (top) and Upa1-Gfp signals (bottom; (**B**)) and the travelled
997 distance of processive Rrm4-Kat (top) and Upa1-Gfp signals (bottom; (**C**); per 10 µm of hyphal
998 length; only particles with a processive movement of > 5 µm were conducted; data points
999 representing mean from n =3 independent experiments, with mean of means, red line and SEM;
1000 unpaired two-tailed Student's t-test ($\alpha<0.05$), for each experiment at least 25 hyphae were
1001 analysed per strain). (**D**) Summary of the *in vivo* analysis shown in Figure 4,5 and EV5A-C.

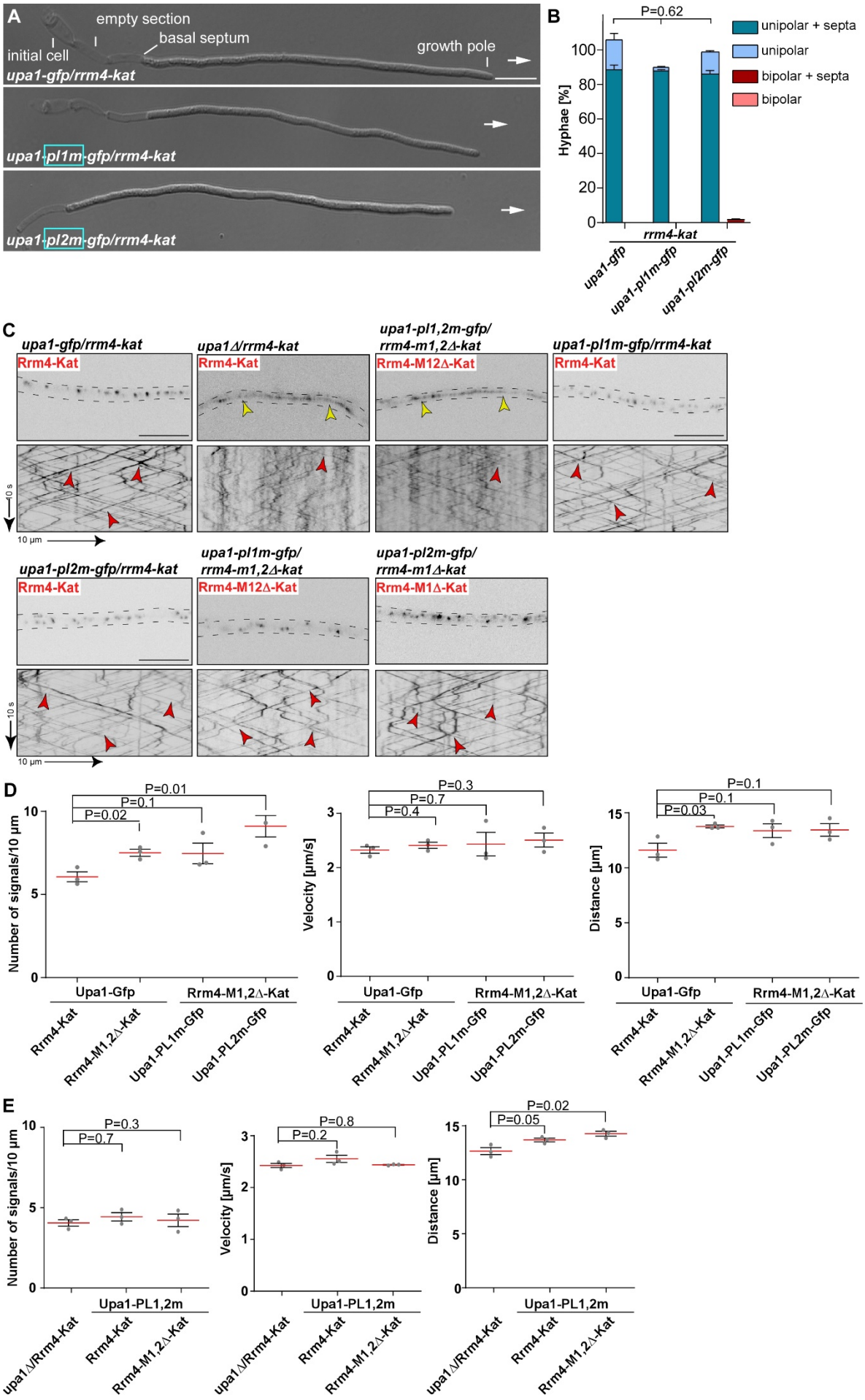
A
empty section
basal septum
initial cell
growth pole
upa1-gfp/rrm4-kat
upa1-pl1m-gfp/rrm4-kat
upa1-pl2m-gfp/rrm4-kat
B
P=0.62
unipolar + septa
unipolar
bipolar + septa
bipolar
Hyphae [%]
rrm4-kat
upa1-gfp
upa1-pl1m-gfp
upa1-pl2m-gfp
C
upa1-gfp/rrm4-kat
Rrm4-Kat
upa1Δ/rrm4-kat
upa1-pl1,2m-gfp/ rrm4-m1,2Δ-kat
Rrm4-M12Δ-Kat
upa1-pl1m-gfp/rrm4-kat
upa1-pl2m-gfp/rrm4-kat
upa1-pl1m-gfp/ rrm4-m1,2Δ-kat
upa1-pl2m-gfp/ rrm4-m1Δ-kat
Rrm4-M1Δ-Kat
10 s
10 µm
D
Number of signals/10 µm
Velocity [µm/s]
Distance [µm]
P=0.01
P=0.1
P=0.02
P=0.3
P=0.7
P=0.4
P=0.1
P=0.1
P=0.03
Upa1-Gfp
Rrm4-M1,2Δ-Kat
Rrm4-Kat
Rrm4-M1,2Δ-Kat
Upa1-PL1m-Gfp
Upa1-PL2m-Gfp
E
P=0.3
P=0.7
P=0.8
P=0.2
P=0.02
P=0.05
Upa1-PL1,2m
upa1Δ/Rrm4-Kat
Rrm4-Kat
Rrm4-M1,2Δ-Kat

1002

1003 **Figure EV5. Deletion of MLLE1^{Rrm4} and -2 cause defects in microtubule association.**

1004 (**A**) Growth of AB33 derivatives in their hyphal form (6 h.p.i.; size bar 10 µm). Growth
1005 direction is marked by arrows. (**B**) Quantification of hyphal growth of AB33 derivatives shown
1006 in panel A (6 h.p.i.): unipolarity, bipolarity and basal septum formation were quantified (error
1007 bars, SEM.; n = 3 independent experiments, > 100 hyphae were analysed per strain; For
1008 statistical evaluation, the percentage of uni- and bipolarity was investigated by using unpaired
1009 two-tailed Student's t-test (α<0.05). (**C**) Micrograph and Kymograph of AB33 hyphae
1010 derivates (6 h.p.i.) expressing red and green fluorescent proteins as indicated. Fluorescence
1011 signals were detected simultaneously using dual-view technology (arrow length on the left and
1012 bottom indicates time and distance, respectively). Processive co-localising signals are marked
1013 by red arrowheads. Aberrant microtubule staining is indicated by a yellow arrowhead. (**D-E**)
1014 Quantification of processive Rrm4-Kat signals (left), velocity of fluorescent Rrm4-Kat (middle)
1015 and the travelled distance of processive Rrm4-Kat signals (right) related to figure 5 C and
1016 EV5C, respectively (per 10 µm of hyphal length; only particles with a processive movement
1017 of > 5 µm were conducted; data points representing mean from n =3 independent experiments,
1018 with mean of means, red line and SEM; unpaired two-tailed Student's t-test (α<0.05), for each
1019 experiment at least 25 hyphae were analysed per strain).